PHOTOEVAPORATION OF DISKS AND CLUMPS BY NEARBY MASSIVE STARS: APPLICATION TO DISK DESTRUCTION IN THE ORION NEBULA

DOUG JOHNSTONE

Canadian Institute for Theoretical Astrophysics, 60 Saint George Street, Toronto, Ontario, Canada, M5S 3H8; johnstone@cita.utoronto.ca

DAVID HOLLENBACH

MS 245-3, NASA Ames Research Center, Moffett Field, CA 94035-1000; hollenbach@warped.arc.nasa.gov

AND

JOHN BALLY

Campus Box 389, Center for Astrophysics and Space Astronomy, Department of Astrophysical and Planetary Sciences, University of Colorado, Boulder, CO 80309; bally@nebula.colorado.edu

ABSTRACT

We present a model for the photoevaporation of circumstellar disks or dense clumps of gas by an external source of ultraviolet radiation. Our model includes the thermal and dynamic effects of 6–13.6 eV far-ultraviolet (FUV) photons and Lyman continuum EUV photons incident upon disks or clumps idealized as spheres of radius r_d and enclosed mass M_*. For sufficiently large values of r_d/M_*, the radiation field evaporates the surface gas and dust. Analytical and numerical approximations to the resulting flows are presented; the model depends on r_d, M_*, the flux of FUV and EUV photons, and the column density of neutral gas heated by FUV photons to high temperatures. Application of this model shows that the circumstellar disks ($r_d \sim 10^{14}–10^{15}$ cm) in the Orion Nebula ("proplyds") are rapidly destroyed by the external UV radiation field.

Close ($d \lesssim 10^{17}$ cm) to θ^1 Ori C, the ionizing EUV photon flux controls the mass-loss rate, and the ionization front (IF) is approximately coincident with the disk surface. Gas evaporated from the cold disk moves subsonically through a relatively thin photodissociation region (PDR) dominated by FUV photons and heated to ~ 1000 K. As the distance from θ^1 Ori C increases, the Lyman continuum flux declines, the PDR thickens, and the IF moves away from the disk surface. At $d \sim 3 \times 10^{17}$ cm, the thickness of the PDR becomes comparable to the disk radius. Between 3×10^{17} cm $\lesssim d \lesssim 10^{18}$ cm, spherical divergence and the resultant pressure gradient in the 10^3 K PDR forms a mildly supersonic (~ 3–6 km s^{-1}) but neutral Parker wind. This wind flows outward until it passes through a shock, beyond which gas moves subsonically through a stationary D-type IF. The IF is moved away from the disk surface to a standoff distance $r_{IF} \gtrsim 2.5 r_d$. In this regime, the mass-loss rate is determined by the incident FUV photon flux and not the ionizing flux. However, at very large distances, $d \gtrsim 10^{18}$ cm, the FUV photon flux drops to values that cannot maintain the disk surface temperature at $\sim 10^3$ K. As the PDR temperature drops, the pressure of the FUV-powered flow declines with increasing distance from θ^1 Ori C, and again the EUV ionizing photons can penetrate close to the disk surface and dominate the evaporation rate.

Radio, Hα, and [O III] observations of externally illuminated young stellar objects in the Trapezium region are used to determine r_{IF} and the projected distances, $d_\perp$, from θ^1 Ori C. The observed values of r_{IF} and $d_\perp$ are combined with the theory to estimate the disk sizes, mass-loss rates, surface densities, and disk masses for the ensemble of extended sources in the Trapezium cluster. Observations of r_{IF}, $d_\perp$, and r_d in HST 182−413 and a few other sources are used to calibrate parameters of the theory, especially the column of heated PDR gas. The disks have a range in sizes between $14 < \log[r_d/(\text{cm})] < 15.2$, mass-loss rates of $-7.7 < \log[\dot{M}/(M_\odot/\text{yr})] < -6.2$, surface densities at disk edge $0.7 < \log[\Sigma(r_d)/(\text{g cm}^{-2})] < 2.5$ which imply disk surface densities at 1 AU from the central, embedded star of $2.8 < \log[\Sigma_0/(\text{g cm}^{-2})] < 3.8$ and disk masses of $0.002 < M_d/M_\odot < 0.07$. Σ and M_d scale with the adopted ionization time, t_i, which we take to be 10^5 yr. The inferred $\Sigma(r_d)$ for the ensemble of disks suggest that the initial surface density power law of an individual disk, $\Sigma \propto r^{-\alpha}$, is bounded by $1 \lesssim \alpha \lesssim 1.5$.

Subject headings: accretion, accretion disks — circumstellar matter — H II regions — ISM: general — open clusters and associations: individual (Orion Nebula Cluster)

1. INTRODUCTION

The quest for proto–planetary disks and clues about the formation of planets has been a major goal of star formation research. The *Hubble Space Telescope* (*HST*) has provided compelling evidence for disks around low-mass young stars in the spectacular images of the Orion Nebula (O'Dell, Wen, & Hu 1993; O'Dell & Wen 1994; Bally et al. 1998c, hereafter Paper I). These pictures show about a half-dozen disks in silhouette against the background light of the Nebula with sizes ranging from 25 to 500 AU, the expected size of proto–planetary disks surrounding young low-mass stars. Furthermore, more than 100 other young stars are surrounded by ionized envelopes with comparable dimensions. There is growing evidence that these stars are also surrounded by circumstellar and possibly proto–planetary disks.

The Trapezium is part of the youngest subgroup (Id) of the Orion OB association. The Trapezium lies about 10–50 pc behind the 3–7 Myr old Ic subgroup ("Orion's Sword"), which in turn lies about 3° south of the older still (5–10 Myr old) Ib subgroup ("Orion's Belt"), which lies south of the dispersed and oldest (10–15 Myr old) Ia subgroup (Blaauw 1991; Bally 1996). The Trapezium region is illuminated by a cluster of four luminous stars whose brightest member, θ^1 Ori C (spectral type O6ep), is responsible for most of the ionization. Infrared images reveal a rich cluster of over 700 young stars packed into a region with a radius of less than 1 pc and a peak stellar density of 5×10^4 pc^{-3} in the central 0.1 pc diameter core (McCaughrean & Stauffer 1994). The age of the Trapezium cluster is of order 1 Myr (Herbig & Terndrup 1986; Prosser et al. 1994; Hillenbrand 1997), determined from Hertzprung-Russell diagrams and evolutionary tracks for the low-mass stars in the cluster. This age estimate is probably an upper limit due to uncertainties in the atmospheric opacities of cool stars and the resulting uncertainties in their pre–main-sequence evolutionary tracks.

Radio continuum observations (Churchwell et al. 1987; Garay, Moran, & Reid 1987; Felli et al. 1993) revealed more than 50 compact (< 200 AU) sources within several arcminutes of the Trapezium. A majority, $\sim 60\%$, have variable, nonthermal spectra and are unresolved. Spread uniformly throughout the cluster, these objects appear similar to photospheric flare stars, with gyrosynchrotron emission being the source of the radio flux. The other 40% of the compact radio objects are slightly extended thermal emitters clustered tightly around θ^1 Ori C. The radio emission is thermal bremsstrahlung at a temperature of $T \sim 10^4$ K and peak electron densities $n_e \sim 10^6$ cm^{-3}. These radio sources were first thought to be photoionizing globules but are now recognized to coincide with low-mass members of the Trapezium cluster.

Optical and infrared observations helped to identify the nature of the compact sources. Laques & Vidal (1978) first identified six of the brightest objects in narrowband images in the Hα line. Most thermal radio sources are extended in the *HST* images and contain central stars in the infrared images (McCaughrean & Stauffer 1994; Stauffer et al. 1994). Conversely, approximately half of the stars seen in the infrared images of the inner portion of the Trapezium cluster have an extended emission in the *HST* images.

Churchwell et al. (1987) recognized that the mass-loss rate observed in the ionized gas implies a neutral reservoir that would obscure the embedded stars if the material were distributed spherically. Therefore, the extended radio emission might be produced by the evaporation of circumstellar disks. The electron density in the compact sources, determined from the radio emissivity, is $n_e \sim 10^6$ cm^{-3}, which is denser than the surrounding nebula by more than a factor of 100. The resulting overpressure should lead to the expansion of a fully ionized condensation on a dynamical time $r/a_{\mathrm{II}} \sim 100$ yr. Therefore, a steady evaporative flow from a dense neutral reservoir must resupply the material as it expands away. If the material flows away at the sound speed in the ionized gas, $a_{\mathrm{II}} \sim 10$ km s^{-1}, the mass-loss rate, $\dot{M}$, is estimated to be $\sim 10^{-7}$ $M_\odot$ yr^{-1} for an object of typical size (200 AU). Maintaining the flow over the ~ 1 Myr lifetime of the region requires a neutral hydrogen reservoir mass of $M > \dot{M} t_{\mathrm{T}} \sim 0.1$ $M_\odot$ which, if distributed spherically, would fully extinguish the central star even at IR wavelengths. Even if the time since first ionization is only 1%–10% of the cluster lifetime, the reservoirs must be stored in a highly flattened configuration to avoid obscuration of the central stars. Since most extended radio and optical sources have central stars visible in near-IR images, severe constraints are placed on the axial ratio of the neutral hydrogen envelope, which strongly suggests that the material is confined to a disk.

O'Dell et al. (1993) resolved the shapes of the extended ionized envelopes with the subarcsecond resolution provided by *HST*. Most sources appear cometary with a bright head facing θ^1 Ori C and elongated tail extending away from the illuminating star. A few sources point toward a second ionizing source, θ^2 Ori A. O'Dell et al. introduced the term "proplyds" as a descriptive name for these objects, believing that they were externally illuminated protoplanetary disks (i.e., PROtoPLanetarY DiskS).

During the Early Release Observations program after the first *HST* servicing mission, O'Dell & Wen (1994) again imaged the Trapezium region. With the enhanced resolution available after the repair mission, 26 new extended sources were discovered, bringing the total number of extended radio and optical objects to over 50. A number of dark silhouettes seen against the bright nebular background were also found. Central stars are visible in the middle of several elliptical objects, suggesting nearly face-on opaque circumstellar disks. Others appear as elongated shapes with nearly constant width and do not contain central stars, even in near-IR images. These may be optically thick disks seen edge-on so that they completely hide their central stars.

Recent *HST* observations have revealed about 150 young stellar objects (YSOs) in the Trapezium region that are surrounded by resolved circumstellar structure (O'Dell & Wong 1996). Most are bright in nebular emission lines, but seven are pure silhouettes that lie in front of the Nebula (McCaughrean & O'Dell 1996; O'Dell & Wong 1996). The pure dark silhouettes either lie sufficiently far from θ^1 Ori C in a region where the flux of ionizing radiation is so low that the emission measure of the IF is lower than that of the nebular background or lie completely outside the Strömgren sphere past the near-side ionization front that caps the Orion Nebula (the so-called "neutral lid"). About 30% of the bright externally illuminated young stellar environments contain dark silhouettes at their centers (see Paper I). The disks seen in silhouette have sharp outer edges, indicating an abrupt decrease in their surface density, which is not consistent with a radial power law with an exponent in the range -0.75 to -1.5 (McCaughrean & O'Dell 1996).

Ground-based adaptive optics observations (McCullough et al. 1995) combined with the earlier radio data reveal that the size of the extended ionized objects scale as $r_{\mathrm{IF}} \propto d^{2/3}$, where d is the distance from the illuminating source. If the mass-loss mechanism is initiated by photoionization at the disk surface and the disk size is constant, then the observed size should be constant since the ionization front should be coincident with the disk. The mass-loss rate should decrease with distance as the Lyman continuum flux rate diminishes, leading to $\dot{M} \propto d^{-1}$, which contradicts the data. As recognized by McCullough, a constant mass-loss rate produces exactly the size versus distance relation observed. In this model, neutral material flows away from the underlying disk until it reaches the

ionization front at a standoff distance, $r_{IF} \propto d^{2/3}$, that is dependent on the incident UV flux. McCullough proposed that photodissociation of molecular hydrogen at the disk surface was the driving mechanism for the constant mass-loss rate but did not elaborate the model further.

Shu, Johnstone, & Hollenbach (1993), Hollenbach et al. (1994), and Johnstone (1995) investigated circumstellar disk evaporation produced by the Lyman continuum (EUV) flux of the star *embedded* within the disk. The standard model for disk destruction requires EUV Lyman continuum photons from the central star to ionize and heat the disk surface to temperatures $T \sim 10^4$, producing an evaporative flow in the outer disk. Close to the center of the disk, the gravitational potential of the star confines the heated gas, producing a hydrostatic disk atmosphere. Beyond a critical distance, r_g, at which the sound speed in the ionized gas roughly equals the escape velocity from the system, the heated material is no longer bound by gravity and escapes as a thermal disk wind. For young high-mass stars, photoevaporation of the circumstellar disk is an efficient destruction mechanism, resulting in mass-loss rates $\dot{M} \sim 10^{-5} M_\odot$ yr^{-1} and producing ultracompact H II regions (Hollenbach et al. 1994; Johnstone 1995). The photoevaporative disk destruction rate decreases dramatically with decreasing stellar mass because low-mass stars produce few ionizing EUV photons. For low-mass protostars, $\dot{M} \sim (10^{-9}$ to $10^{-10})~M_\odot$ yr^{-1}. Nevertheless, the extended lifetime of these star-disk systems allows a significant amount of disk material to be evaporated, with possible consequences for the hydrogen content of outer giant planets (Shu et al. 1993; Johnstone 1995).

The external radiation field in the Orion Nebula evaporates circumstellar disks much faster than the radiation field of the low-mass star within each disk. Treatment of disk destruction by external sources requires a different geometry and theoretical approach. Despite this, some of the essential features of the older work, such as the concept of a critical radius, r_g, remain valid. An upper bound on the lifetime of the bright extended sources in the Orion Nebula is provided by the age of the Trapezium region, $t_T \lesssim 10^6$ yr. Once ionizing radiation from the high-mass stars invaded the parent cloud, star formation would have been effectively halted. Thus, the age of the Orion Nebula must be less than the median age of the low-mass stars contained within. θ^1 Ori C shows peculiarities that may be an indication of extreme youth (see Gagné et al. 1997), which implies that an ionization age as low as $t \sim 10^4$ yr is not ruled out. Throughout this paper, we settle on an ionization time of $t_i = 10^5$ yr as an estimate of the evaporation age of the circumstellar disks in the Orion Nebula.

In this paper, we present a general model for EUV and far-ultraviolet (FUV) photoevaporation of disks and clumps and apply the model to the proplyds in the Orion Nebula. Section 2 describes the theoretical model for evaporation of disks/clumps by an external source of FUV (6 eV $< h\nu <$ 13.6 eV) and EUV Lyman continuum photons. In § 3, the model is calibrated using the star-disk system HST 182−413 (HST 10) and the results used to compute disk parameters for the ensemble of extended sources in the Trapezium cluster. We use the model to estimate disk sizes, mass-loss rates, surface densities, and disk masses and compare these results with other estimates of disk properties. Finally, in § 4 we summarize the results and present conclusions.

2. THEORY OF DISK PHOTOEVAPORATION BY AN EXTERNAL SOURCE

2.1. Overview

Two distinct heating mechanisms may initiate photoevaporation. EUV photons ($h\nu > 13.6$ eV; $\lambda < 912$ Å) ionize gas and raise its temperature to about $T \sim 10^4$ K. FUV photons (6 eV $< h\nu <$ 13.6 eV; $\lambda > 912$ Å) dissociate molecules and heat the photodissociation region (PDR) gas to about $T \sim 100$–1000 K but leave it predominantly neutral. While EUV photons cannot penetrate the ionization front (IF), the FUV photons, which are not absorbed by atomic hydrogen, penetrate and heat the neutral gas. For FUV fluxes in the range $G_0 \sim 10^4$–10^6 (where G_0 is in units of "Habing" flux, the estimated average flux in the local interstellar medium, taken to be 1.6×10^{-3} ergs cm^{-2} s^{-1}) that are encountered in the central regions of the Orion Nebula, the PDR is heated to a temperature of order $T \sim 1000$ K (Tielens & Hollenbach 1985). The gas is heated primarily by photoelectrons ejected from grains and by H$_2$ FUV pump heating. Since dust is the primary source of attenuation of the FUV photons, the column density of the photoheated PDR is determined by the condition that the dust optical depth is about $\tau_{FUV} \sim 1$–3. The chemistry, heating, FUV penetration, and spectra of FUV-induced flows are further studied in Hollenbach & Störzer (1998).

In EUV-dominated flows, thermal pressure at the disk surface is determined by photoionization, and the FUV-produced PDR remains relatively thin ($\Delta r \lesssim r_d$). FUV-heated neutral gas moves subsonically through this thin layer toward the IF, and the mass-loss rate is controlled by the EUV-induced ionization rate.

In FUV-dominated flows, the thermal pressure at the disk surface is determined by the FUV heating. The warm neutral gas expands and is launched from the surface of the disk as a thermal wind. The supersonic wind pushes the IF away from the disk surface. The mass-loss rate is determined by the PDR temperature, the FUV flux, and the FUV dust opacity. The mass-loss rate is a weak function of the FUV flux for $G_0 \sim 10^4$–10^6, since the PDR temperature does not strongly depend on G_0 in this range.

While the geometry near the disk produces an initially cylindrical flow, the pressure gradient reorients this wind into a spherical flow that is accelerated by the radial pressure gradient into a Parker wind. Figure 1 shows schematically the shape of the streamlines expected for either EUV- or FUV-heated disk winds. In our models, we assume spherical "disks" of radius r_d illuminated by external sources of EUV and FUV photons. Note that the outer disk edge is at r_d, and the flow is cut off at an inner radius, r_g, by gravity.

The continuity equations for mass and momentum flux across the IF constrain the neutral flow velocity entering the IF. Beyond the IF, overpressure of the gas produces supersonic expansion in the ionized medium at speeds of order $(1$–$2)a_{II}$, where a_{II} is the sound speed in the H II region. Two possible steady state solutions exist for neutral flow into the IF. Either the flow has high Mach number, $v_I/a_I > 2a_{II}/a_I$, producing a rarefied (R-type) ionization front with little density contrast across the front, or the neutral flow is subsonic, $v_I/a_I \sim a_I/(2a_{II})$, producing a D-type front with a large density contrast across the front (Spitzer 1978). Here a_I is the sound speed on the PDR side of the IF. With no available mechanism for reaching a high Mach number in
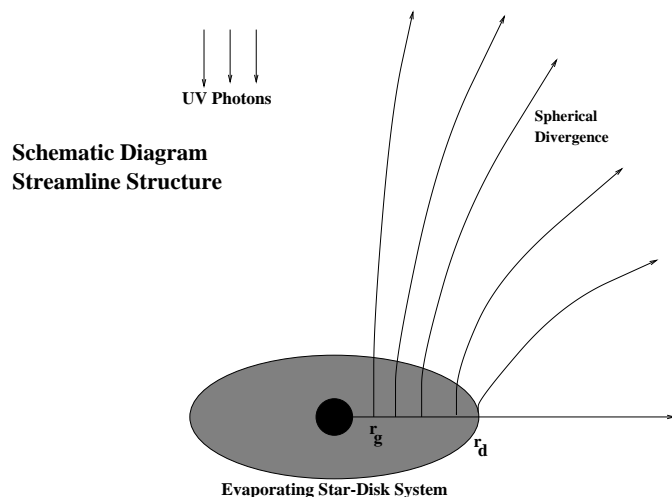
FIG. 1.—Schematic diagram for the evaporating star-disk systems discussed in the text showing the structure of the streamlines leaving the disk surface. While the disk imposes a cylindrical geometry on the streamlines as they leave the surface, pressure in the atmosphere should quickly lead to a spherical flow. The inner cutoff for flow occurs at $0.5r_g$, the position at which thermal expansion is halted due to the gravitational potential of the central star (see text).

the neutral medium, the flow velocity is restricted to be subsonic (D-type) on the neutral side of the boundary. With $a_I \sim 3$ km s^{-1} in the ~ 1000 K neutral gas and $a_{II} \sim 10$ km s^{-1} in the ionized gas, the neutral gas flows into the IF with a velocity $v_{IF} \sim 0.5$ km s^{-1}.

In the case of EUV-dominated flows where the PDR region is thin, the PDR flow is everywhere subsonic, which allows the thermal pressure to equilibrate and produces approximately constant density gas in the nearly isothermal PDR. To conserve mass flux, $v_I \propto r^{-2}$ and declines to 0.5 km s^{-1} as r increases from r_d to r_{IF}. However, in the case of FUV-dominated flows, the PDR flow is initially $v_I \sim a_I \sim 3$ km s^{-1}, and pressure gradients increase the flow velocity to supersonic values, $v_0/a_I \sim 1$–2, producing a neutral Parker wind. The neutral gas must then pass through a shock, be decelerated, move subsonically through an isobaric shell where $v_I \propto r^{-2}$, and finally pass through the IF at $v_{IF} \sim 0.5$ km s^{-1}. These solutions are described in detail in §§ 2.2 and 2.3 below.

For either heating mechanism, an evaporative flow can only exist if the thermal pressure exceeds the local gravity. Thus, an evaporative disk wind can exist only beyond a critical radius, r_g. Inside r_g, the photoheating produces a warm, static disk atmosphere held in place by the gravitational well of the central star. The value of r_g can be estimated by balancing the energy required to escape a Keplerian orbit with the thermal energy, resulting in

$$r_g = \frac{GM_*}{a^2}, \tag{1}$$

where a is the sound speed in the gas. In ionized EUV-dominated flows, $a_{II} \sim 10$ km s^{-1}, while in neutral FUV-dominated flows, $a_I \sim 3$ km s^{-1}. Thus, for a typical star in the Trapezium cluster with $M_* = 0.2\ M_\odot$ (Hillenbrand 1997), the gravitational radii are $r_{gII} \sim 2.5 \times 10^{13}$ cm (~ 2 AU) and $r_{gI} \sim 2.5 \times 10^{14}$ cm (~ 20 AU).

These critical radii overestimate the size of the remnant disks that might survive photoevaporation. In the Parker wind problem (Parker 1963; Shu 1991), material launched at the sound speed from a depth of $0.5r_g$ escapes the stellar potential due to the pressure gradient in the divergent flow. Woods et al. (1996) found considerable flow from well within r_g (as close as $0.2r_g$) in their simulation of Compton heated disk winds. Thus, we consider it likely that photoevaporation of the disk ends when the disk outer radius reaches a value close to $0.5r_g$ but recognize this value could be as small as $0.2r_g$.

Observations of the externally ionized YSOs in the Trapezium cluster demonstrate that in many cases EUV photons *do not* reach the disk surface and may therefore not be directly responsible for disk evaporation. In Paper I we demonstrate that the ionization fronts surrounding most evaporating sources are hemispherical. If the ionization front were located at the disk surface, then the IF would appear round only for disks seen pole-on. Disks oriented edge-on or at intermediate angles with respect to our line of sight would exhibit either flat or elliptical IFs with significant asymmetries, contrary to the observations. In the larger evaporating sources, where the disks can be seen either in silhouette or in [O I] emission, the disks have radii several times smaller than the radii of the associated IFs (see Fig. 8 for an outstanding example). The mass-loss rate resulting from direct ionization of the disk surface is expected to vary strongly with distance from θ^1 Ori C. This is not observed. Ionization fronts coincident with the disk surfaces would be expected to yield source sizes proportional to the disk radius. Observations (see § 3) show that the ionization front radii increase with distance from θ^1 Ori C. This is more naturally explained by the increase of the standoff distance of the IF caused by neutral FUV-induced flows than by a systematic increase in disk radii with increasing distance from θ^1 Ori C. However, such a variation may result from the more rapid erosion of the lower surface density outer portions of disks near the UV source.

In the following sections (§§ 2.2–2.4), we model the combined effects of EUV and FUV photons and find two distinct regimes: FUV-dominated and EUV-dominated flows.

2.2. *Analytic Treatment of FUV-Dominated Flows*

Neutral wind outflows can occur only from disks larger than $r_d \gtrsim 0.5r_{gI}$, which is roughly 10^{14} cm for 0.2 $M_\odot$ central stars (eq. [1]). Equivalently, the condition can be written

$$\frac{r_d}{M_*} \gtrsim \left(\frac{5 \times 10^{14}\ \mathrm{cm}}{M_\odot} \right). \tag{2}$$

In the following, we assume that this minimal condition holds. Figure 2 presents a schematic diagram of a simple model for which analytic solutions may be found that illustrate the structure and parameter dependence of FUV-dominated flows. Supersonic flow at constant speed v_0 (roughly 1–$2a_I$, or 3–6 km s^{-1}) is assumed to emerge from a spherical "disk" of radius r_d. The density at the flow base ($r = r_d$) is n_0. The density drops as r^{-2}, conserving mass flux, until the neutral wind hits a shock front (SF) at r_s. Assuming an isothermal shock, the density jumps by a factor $\sim M^2$ across the SF, where $M = v_0/a_I$ is the Mach number. Between the SF and the IF, the PDR flow is subsonic and the gas is assumed isobaric and isothermal, so the
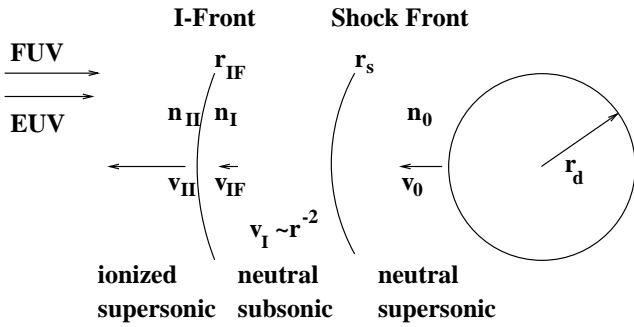
FIG. 2.—Schematic diagram showing the three distinct regions through which FUV-dominated flows pass. Neutral material is launched at v_0 (1–2 times the sonic speed) from the disk, passes through an isothermal shock producing a subsonic flow, and is ionized across the ionization front.

density is roughly constant. The PDR flow velocity decreases to v_0/M^2 across the SF and then decreases as r^{-2} through the shell between the SF and the IF, conserving mass flux. The velocity of the PDR flow through the IF is $v_{IF} = a_I^2/(2a_{II})$, in order to conserve mass and momentum flux through the IF. Solution of these mass and momentum constraints results in

$$r_s = \left(\frac{v_0}{2a_{II}}\right)^{1/2} r_{IF} . \qquad (3)$$

Since $v_0 \sim 3$–6 km s^{-1} and $a_{II} \sim 10$ km s^{-1}, $r_s \sim (0.4$–$0.6)r_{IF}$; the shock front is roughly halfway between the IF and the disk.

The column density of the warm PDR gas between the disk surface and the IF is set by the dust opacity, $\tau_{FUV} \sim 1$–3. We take this fiducial column density to be $N_D \sim (1$–3$) \times 10^{21}$ cm^{-2}, dependent on the dust properties and the penetration of sufficient FUV photons to maintain the gas temperature at $T \sim 1000$ K (Hollenbach & Störzer 1998). The incident ionizing EUV flux is mainly absorbed by dust and (recombined) hydrogen atoms in the ionized flow, with the rest absorbed by the ionization of matter streaming through a stationary IF at the base of the ionized flow (Bertoldi & McKee 1990; Hollenbach et al. 1994). If $r_{IF} > (v_0 a_{II}/a_I^2)r_d \sim (3$–6$)r_d$, the column density in the PDR flow region is dominated by the column in the diverging supersonic wind, which is dominated by the column at the base,

$$N_D \simeq n_0 r_d . \qquad (4)$$

The mass-loss rate is given by the density at the base and the flow speed, or

$$\dot{M} = 4\pi r_d^2 v_0 n_0 m_I , \qquad (5)$$

where $m_I = 1.35 m_H$ is the mean particle mass per hydrogen atom. This equation can be immediately solved to find that the mass-loss rate grows in direct proportion to the disk size:

$$\dot{M} = 1.3 \times 10^{-8} \epsilon r_{d14} \; M_\odot/\text{yr} , \qquad (6)$$

where

$$\epsilon = \left(\frac{N_D}{10^{21} \; \text{cm}^{-2}}\right)\left(\frac{v_0}{3 \; \text{km s}^{-1}}\right) \qquad (7)$$

is a dimensionless parameter of order unity that subsumes our uncertainty in N_D and v_0, and $r_{d14} = r_d/10^{14}$ cm.

Provided that the disk is large enough to produce a warm thermal disk wind, $r_d \gtrsim 0.5 r_{gI}$, and assuming an FUV-dominated flow, the mass-loss rate is relatively independent of the distance to the UV source, d. However, there is in fact some mass-loss rate dependence on d because the PDR temperature, and hence v_0, does depend on distance from the photon source, although the dependence is weak for $G_0 \sim 10^4$–10^6 or $d \sim 10^{17}$–10^{18} cm around θ^1 Ori C (Tielens & Hollenbach 1985; Hollenbach & Störzer 1998).

The IF standoff distance, r_{IF}, can be calculated for this fixed mass-loss rate. Let f_r be the fraction of EUV photons absorbed by recombinations in the ionized portion of the flow [$(1 - f_r)$ is roughly the fraction absorbed by dust and the background nebula]. Balance between recombinations and ionizations, along with continuity of flow, requires

$$\frac{f_r \Phi_i}{4\pi d^2} = \frac{\alpha_r n_0^2 r_{IF}}{3}\left(\frac{v_0}{a_{II}}\right)^2\left(\frac{r_d}{r_{IF}}\right)^4 , \qquad (8)$$

where $\alpha_r = 2.6 \times 10^{-13}$ cm^3 s^{-1} is the recombination coefficient for hydrogen at 10^4 K, and Φ_i is the EUV photon luminosity of the UV source ($\Phi_i \sim 10^{49}$ s^{-1} for θ^1 Ori C). Substituting N_D/r_d for n_0 and rearranging yields

$$r_{IF} = \left[\frac{\alpha_r N_D^2}{3 r_d}\left(\frac{v_0}{a_{II}}\right)^2\left(\frac{4\pi d^2}{f_r \Phi_i}\right)\right]^{1/3} r_d . \qquad (9)$$

This equation is valid for $r_{IF} > (v_0 a_{II}/a_I^2)r_d$ or $(3$–6$)r_d$. Substituting typical values gives

$$r_{IF14} = 0.975 \left(\frac{\epsilon^2}{f_r \Phi_{49}}\right)^{1/3} r_{d14}^{2/3} d_{17}^{2/3} , \qquad (10)$$

where $r_{IF14} = r_{IF}/10^{14}$ cm, $\Phi_{49} = \Phi_i/10^{49}$ s^{-1}, and $d_{17} = d/10^{17}$ cm. This is the result first recognized by McCullough et al. (1995); if the neutral mass-loss rate is constant with distance, d, from the ionizing source, then the IF standoff distance, r_{IF}, increases with $d^{2/3}$. Here, however, we have added the physics of the neutral flow, derived the mass-loss rate, and found that the flow requires a shock and a neutral subsonic shell between r_s and r_{IF}. In § 3 we show that calibration with observations indicate $\epsilon/(f_r \Phi_{49})^{1/2} \sim 4$ and thus the fiducial values for N_D and v_0 and the approximated flow geometry are likely reasonable estimates.

Equation (9) shows that as the ionizing flux [$f_r \Phi_i/(4\pi d^2)$] incident on the disk increases, r_{IF} and r_s decrease and approach r_d. For the narrow range $(2a_{II}/a_I)^{1/2} r_d < r_{IF} < (v_0 a_{II}/a_I^2)r_d$, or roughly $2.5 r_d \lesssim r_{IF} \lesssim 4r_d$, a shock and subsonic shell still persist outside of r_d, *but the shell dominates the column density* and

$$N_D \simeq \frac{n_0 r_{IF}}{2}\left(\frac{2v_0 a_{II}}{a_I^2}\right)\left(\frac{r_d}{r_{IF}}\right)^2 . \qquad (11)$$

Combining this equation with equation (8) yields

$$r_{IF} = \frac{\alpha_r N_D^2}{3}\left(\frac{4\pi d^2}{f_r \Phi_i}\right)\left(\frac{a_I}{a_{II}}\right)^4 , \qquad (12)$$

or, inserting typical values,

$$r_{IF14} \simeq 0.1\left(\frac{\epsilon^2}{f_r \Phi_{49}}\right)d_{17}^2 . \qquad (13)$$

The standoff distance now scales with d^2 and decreases sharply as the ionizing flux increases.

Finally, for sufficiently high incident EUV flux, or equivalently for sufficiently small d, the EUV dominates the flow, $r_{IF} \lesssim (2a_{II}/a_I)^{1/2} r_d \sim 2.5 r_d$, and no shock or supersonic neutral flow exists. We shall treat this case in the next section. Here we note that the criteria for the existence of a shock and an FUV-dominated flow can be written, using equation (12), as

$$d > d_{min} = \left(\frac{2a_{II}}{v_0}\right)^{1/4} \left(\frac{a_{II}}{a_I}\right)^2 \left(\frac{3r_d}{\alpha_r N_D^2}\right)^{1/2} \left(\frac{f_r \Phi_i}{4\pi}\right)^{1/2} . \quad (14)$$

Substituting typical values,

$$d_{min} \simeq 5 \times 10^{17} \left(\frac{\epsilon^2}{f_r \Phi_{49}}\right)^{-1/2} r_{d14}^{1/2} \text{ cm} . \quad (15)$$

Equation (14) can be rewritten equivalently as a condition on the size of a disk or clump that will support FUV-dominated flows,

$$r_{d14} \lesssim 0.03 \left(\frac{\epsilon^2}{f_r \Phi_{49}}\right) d_{17}^2 . \quad (16)$$

Therefore, FUV-dominated flows exist primarily for small clumps or disks illuminated by relatively weak EUV fluxes.

However, it is very important to realize that FUV-dominated flows can only exist if there are sufficient FUV photons to heat the gas to escape temperatures. Therefore, the disks cannot be too small (see eq. [1]) or too far away from the ionizing source. The PDR results of Tielens & Hollenbach (1985) and Hollenbach & Störzer (1998) suggest that $G_0 \gtrsim 10^4$ is required to heat the gas to $T \sim 1000$ K. Define f_{FUV} such that $\Phi_{FUV} = f_{FUV} \Phi_i$; $f_{FUV} \sim 1$ for O stars and $f_{FUV} > 1$ for B stars and later (Bertoldi & Draine 1996). Then the heating criterion transforms to a maximum value of d for FUV-induced flows of

$$d < d_{max} \sim 10^{18} f_{FUV}^{1/2} \Phi_{49}^{1/2} \text{ cm} . \quad (17)$$

For $d > d_{max}$, the EUV photons again penetrate to near the disk surface, as now $r_d < r_{gI}$ for PDR flow (the PDR is too cool to evaporate) and EUV-dominated flow resumes. Thus, EUV dominates the flow for both high and low UV fluxes.

Comparison of criterion (14) with criterion (17) shows that there is a relatively narrow range of d, $d_{min} < d < d_{max}$, or equivalently a narrow range of UV flux, which results in FUV-dominated flows. This range increases with increasing N_D, v_0, and f_{FUV} and with decreasing r_d. It depends on the details of the FUV penetration of the PDR and the FUV heating. Hollenbach & Störzer (1998) will present a detailed study, utilizing time-dependent PDR codes, of the heating and chemistry in evaporative flows in order to more accurately determine the available parameter space for FUV-dominated flows. In this paper, we shall assume $d_{max} = 10^{18}$ cm for the evaporating sources in Orion and utilize the observations to normalize the value of $\epsilon/(f_r \Phi_{49})^{1/2}$, which sets d_{min}.

2.3. Analytic Treatment of EUV-Dominated Flows

The criteria above ($d < d_{min}$, $d > d_{max}$, or $r_{gII} < r_d < r_{gI}$) describe when the EUV flux dominates the flow characteristics. Figure 3 presents a schematic of the structure of EUV-dominated flows. In this case, the flow through the PDR is subsonic. For our assumed isothermal conditions, the density, n_I, is constant in the PDR. However, to con-
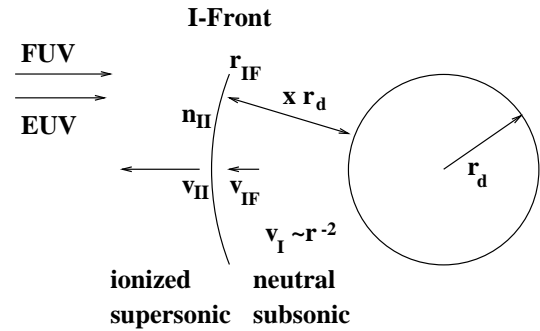

FIG. 3.—Schematic diagram showing the two distinct regions through which EUV-dominated flows pass. Neutral material is launched at subsonic speed from the disk and is ionized across the ionization front.

serve mass, the velocity, v_I, through the PDR decreases as r^{-2} until it reaches $v_{IF} = [a_I^2/(2a_{II}) \sim 0.5]$ km s^{-1} at the IF.

If we denote the thickness of the PDR layer as $x r_d$, the density in the PDR is given by

$$n_I = \frac{N_D}{x r_d} . \quad (18)$$

We have seen in § 2.2 that $x \lesssim 1.5$ ($r_{IF} \lesssim 2.5 r_d$) for EUV-dominated flows. The mass-loss rate through the IF is just

$$\dot{M} = 4\pi (1 + x)^2 r_d^2 n_I m_I \left(\frac{a_I^2}{2a_{II}}\right) . \quad (19)$$

Substituting for n_I and typical values yields

$$\dot{M} = 2.0 \times 10^{-9} \frac{(1 + x)^2}{x} \epsilon r_{d14} \ M_\odot \text{ yr}^{-1} , \quad (20)$$

where the factor ϵ contains all of our uncertainties, most importantly those in $N_D/10^{21}$ cm^{-2} and the flow geometry, and is expected to be of order unity. The neutral layer thickness, x, allows for a range of mass-loss rates, increasing without bound as $x \to 0$. However, there is an additional equation that must be satisfied: the incident EUV flux not absorbed by dust must be able to penetrate to the IF, or

$$\frac{f_r \Phi_i}{4\pi d^2} = \int_{r_{IF}}^{\infty} \alpha_r n_{II}^2(r) dr . \quad (21)$$

This reduces to a defining equation for x:

$$\frac{x}{(1 + x)^{1/2}} = 0.21 \left(\frac{\epsilon^2}{f_r \Phi_{49}}\right)^{1/2} \left(\frac{d_{17}^2}{r_{d14}}\right)^{1/2} . \quad (22)$$

Thus, the EUV sets the pressure that sets x or the PDR density, n_I. Note that for $x \ll 1$, we obtain

$$\dot{M} = 9.5 \times 10^{-9} f_r^{1/2} \Phi_{49}^{1/2} d_{17}^{-1} r_{d14}^{3/2} \ M_\odot \text{ yr}^{-1} , \quad (23)$$

which is the well-known solution for the evaporation of spheres of size r_d by EUV photons, ignoring the effects of the PDR (Bertoldi & McKee 1990). The mass-loss rate scales as d^{-1}, unlike the FUV-dominated regime. For $x \sim 1$ it is interesting that, although the EUV still determines the pressure, the passive PDR does affect the mass-loss rate, increasing it by $(1 + x)^2$, or of order 4. In this case, the finite size of the PDR significantly increases the size of the neutral clump being evaporated by the EUV flux, leading to higher $\dot{M}$.

2.4. *Numerical Model of Evaporation*

In order to more accurately quantify the results of the proceeding section, numerical calculations have been performed following the Parker wind model (Parker 1963; Shu 1991). Gravity is included by assuming that each disk contains an embedded star with mass $M_* = 0.2\ M_\odot$. The corresponding gravitational radius for the neutral gas is $r_{gI} = 2.5 \times 10^{14}$ cm (eq. [1]). In the numerical model, the disk is replaced by a sphere with radius r_d and the neutral flow velocity is fixed at the ionization front location, r_{IF}, to satisfy the ionization front jump conditions; $v_{IF} = a_I^2/(2a_{II})$. The model ignores internal dynamical disk properties such as angular momentum. This should not be a significant source of error for disks with $r_d \geq r_g$.

The equation of continuity requires that all points in the steady neutral flow obey the conservation of mass:

$$C_1 = n_I v_I r^2 \ , \tag{24}$$

where C_1 is a constant whose absolute value is determined through consideration of the column density in the neutral flow. Conservation of momentum provides a second constraint which may be written in the form of the Bernoulli equation,

$$C_2 = 0.5 v_I^2 + a_I^2 \log{(n_I)} - \frac{GM_*}{r} \ . \tag{25}$$

This equation breaks down across shock fronts, since energy and entropy are not conserved. However, we apply isothermal shock jump conditions across r_s, and the required Bernoulli equation upstream from the shock can be computed by consideration of the velocity and density jump across the front and the nonaffected equation of continuity (eq. [24]).

Numerical solutions for the flow conditions and column density have been computed over a grid of r_d and r_{IF} boundary values. As discussed in the preceding sections, pressure in the ionized flow forces the neutral flow to slow down before reaching the ionization front. Some of the solutions require a shock to accomplish this. The location of the shock is not arbitrary; it is fixed by the requirement of the jump conditions across the shock front and the fixed velocities at r_d and r_{IF}. The simple model employed allows absolutely no freedom in the flow parameters, analogous to our analytic solutions described in §§ 2.2 and 2.3.

Three typical solutions to the flow through the neutral regions for disks of size $r_d = 4r_g$ are presented in Figures 4–6. The first model reproduces a subsonic, isobaric solution of EUV-dominated flows (Fig. 4). The velocity is shown to decrease with increasing radius, reaching $v_I/a_I = \frac{1}{6}$, or $v_I \sim 0.5$ km s^{-1} at the ionization front. The density remains approximately constant, and the column density increases linearly. Model 2 (Fig. 5) shows the result of a supersonic neutral flow (FUV-dominated) in which the column density is determined by the shocked neutral layer. The flow begins at the sonic velocity and increases with radius, while the density decays until reaching a mild isothermal shock. The shock location is determined by the downstream boundary requirement. After passing through the shock, the velocity decreases, and the density remains approximately constant. The column density in this model is dominated by the dense neutral layer between the shock and the IF. The third model (Fig. 6) reproduces supersonic neutral flow (FUV-dominated) in which the column density is dominated by
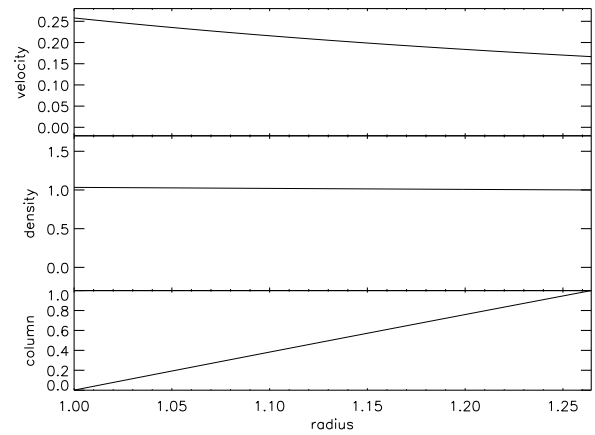

FIG. 4.—Subsonic flow in the neutral layer for a disk with size $r_d = 10^{15}$ cm. *Top*: Neutral flow velocity in units of the sound speed vs. position in units of r_d. The left edge of the plot corresponds to the surface of the disk, while the right edge represents the location of the ionization front. The embedded star is assumed to have mass $M_* = 0.2\ M_\odot$ such that $r_g = 2.5 \times 10^{14}$ cm and $r_d = 4r_g$. The flow velocity is required to be $v_I/a_I = \frac{1}{6}$ ($v_I \simeq 0.5$ km s^{-1}) at the ionization front, which is located at $r_{IF} \sim 1.26 r_d$. The velocity decreases with radius such that the density remains approximately constant. *Middle*: Density normalized to unity at the ionization front. *Bottom*: Cumulative column through the neutral layer as a function of radius. Note that the column increases linearly.

the column near the base. The velocity and density resemble model 2 except that the shock has moved farther from the disk and become stronger. Note that in both Figures 5 and 6 the pressure gradients increase the neutral wind speed to $v_0 \sim (2\text{--}3)v_I$ by the time it reaches the shock front.

Mass-loss rates for each model can be determined by requiring that the column density through the warm neutral medium be $N_D \sim 10^{21}$ cm^{-2}. This requirement fixes the number density of neutral hydrogen at all locations in the flow and, combined with the known velocity field, provides a calibrated solution for the equation of continuity (eq. [24]). The results of the numerical model will be discussed further in § 3, where the measured sizes of the ionization front and disk surrounding HST 182$-$413 are used to cali-
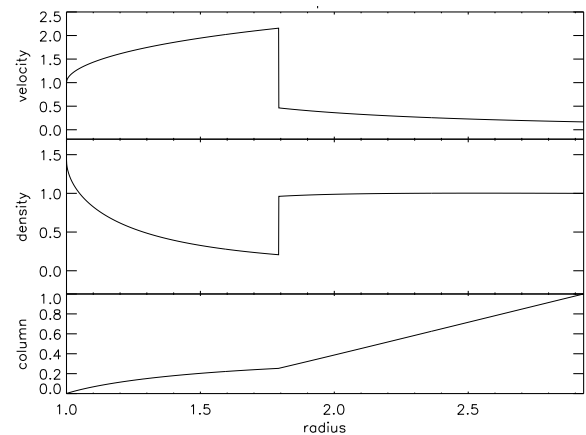

FIG. 5.—Supersonic flow with a thick shocked layer. The plots and units are the same as those in Fig. 4, except that now the ionization front is offset farther from the disk surface, implying a neutral sonic evaporation from the disk. Note that the flow speed increases with radius until producing a mild shock. Upstream from the shock, the density remains approximately constant, and the flow velocity decreases to $v_I/a_I = \frac{1}{6}$ at $r_{IF} \sim 2.9 r_d$. The cumulative column shows that most of the optical depth through the neutral medium is produced in the shocked shell.
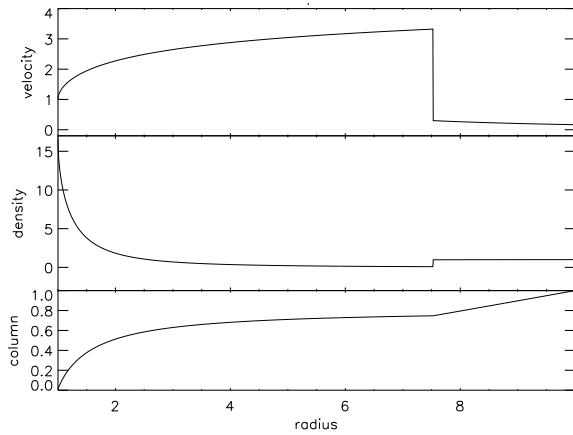
FIG. 6.—Supersonic flow independent of distance. The plots and units are the same as those in Figs. 4 and 5, except that the ionization front is even farther offset from the disk surface, $r_{IF} \sim 10r_d$. The supersonic flow has reached beyond Mach 3 before shocking and creating a constant density shell. The column density is dominated by the flow at the base and thus is approximately independent of the ionization front position. This result indicates that the mass-loss rate is unaffected by the distance from the ionization source.

brate N_D. The properties of the other observed evaporating disk systems are then computed and discussed in relation to the analytic results of §§ 2.2 and 2.3.

2.5. Shape of the Ionization Front

Along with the perpendicular standoff distance, r_{IF}, of the ionization front, the shape of the ionization front can be computed. The shape of the front hemisphere facing θ^1 Ori C is calculated utilizing the geometry and coordinate system shown in Figure 7. In this model, the flux of ionization radiation arrives plane parallel to the evaporating star-

disk system at an impact parameter, y, with respect to the center of evaporation, and this flux reaches a perpendicular distance, x, from the disk before being halted.

Assuming that the density in the ionized gas drops as the square of the distance from the center of evaporation (i.e., the flow is approximately spherically symmetric), the perpendicular distance, x, to the ionization front satisfies

$$\frac{f_r \Phi_i}{4\pi d^2} = \alpha_r n_{IIi}^2 r_{IF} \int_x^\infty \frac{dx}{(x^2 + y^2)^2} , \qquad (26)$$

where n_{IIi} is the electron density at the IF. In the above, x and y are in units of r_{IF}, the standoff distance directly between the ionization source and the evaporating disk. Thus, when $y = 0$, the perpendicular standoff distance is by definition $x = 1$, and the integral integrates to $\frac{1}{3}$. Since the left-hand side and the coefficients of the right-hand side are assumed constant for a given evaporating system,

$$\int_x^\infty \frac{dx}{(x^2 + y^2)^2} = \frac{1}{3} . \qquad (27)$$

The width of the ionization front is measured at the location of the front where $x = 0$. Substituting this into the above integral and solving for the impact parameter reveals $y = 1.3$. Thus, the expected ionization front width, r_w, at the position of the star and under the assumption of spherically symmetric outflow should be

$$r_w = 1.3 r_{IF} . \qquad (28)$$

This is likely a slight overestimate of the actual width of the ionization front since it neglects the diffuse radiation field of the H II region.

We speculate that when comet-like tails are observed, the shape of the ionization front on the "tail" side of the disk
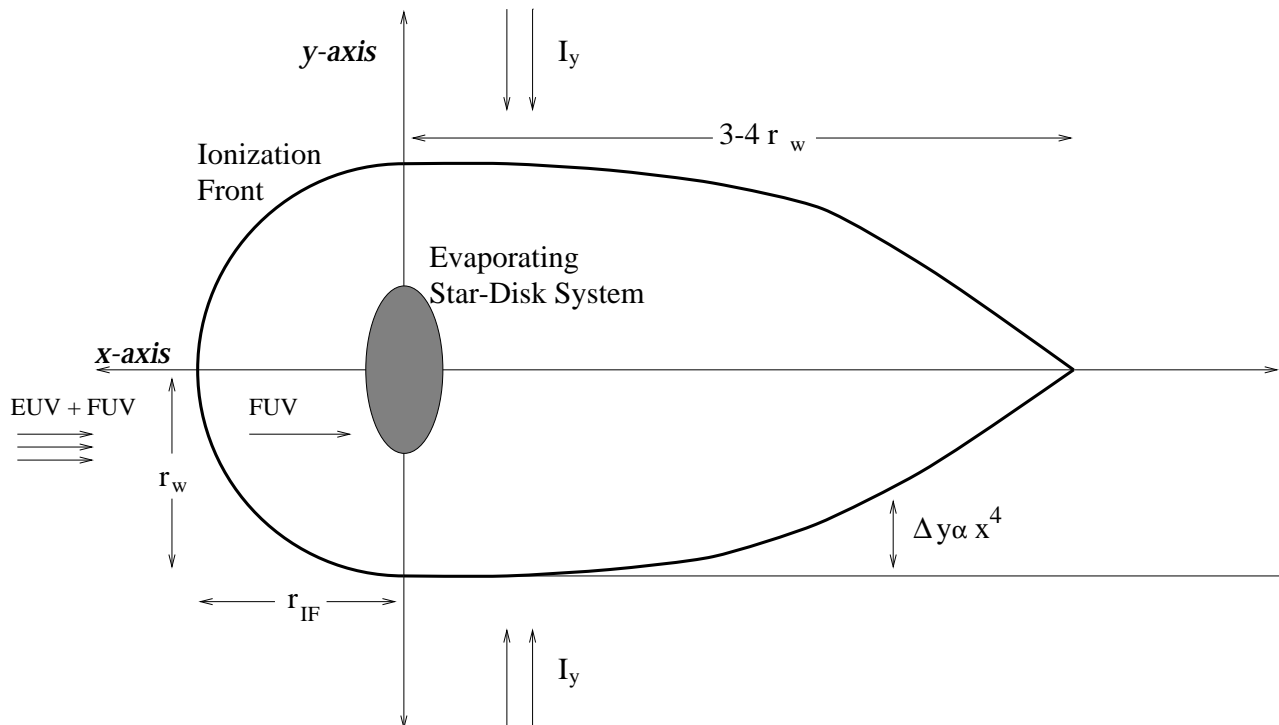

FIG. 7.—Schematic diagram for the formation of a hemispherical ionization front and an ionized tail behind each evaporating source. Diffuse FUV photons heat the disk surface, producing a neutral flow, while diffuse EUV photons penetrate deeper with increasing distance along the shadow axis behind the source.

away from θ^1 Ori C is determined by the diffuse EUV radiation field acting on an FUV-dominated neutral flow. The diffuse FUV field initiates a neutral flow on the backside of the disk, which is similar to that on the front side, although slightly weaker since the diffuse FUV flux is weaker than the direct flux (but recall that the neutral flow is not very sensitive to the FUV flux over a significant range). The diffuse FUV field is caused by dust scattering of FUV as well as the conversion of EUV to FUV via recombinations of hydrogen and helium, with Lyα especially significant. The geometry envisioned is shown in Figure 7, where a shadowed cylinder of radius r_w is pictured behind the disk away from θ^1 Ori C. Let y be the distance from the axis of the cylinder and x be the distance along the cylinder axis. The incident diffuse EUV flux on this cylinder is created by dust scattering and the recombinations of hydrogen and helium above the cylinder; roughly one-third of all hydrogen recombinations are to the ground state, leading to an EUV photon. Ignoring dust scattering, the minimum incident diffuse EUV flux, F_y, is then given roughly as $F_y \simeq \pi I_y$, where

$$I_y \sim \frac{1}{4\pi}\left(\frac{1}{3}\alpha_r n_{ea}^2 y_{II}\right), \tag{29}$$

where n_{ea} is the electron density in the ambient Orion H II region, and y_{II} is the y-distance to the edge of the H II region. Let Δy be the distance of the IF from the cylinder wall (beyond which direct EUV flux dominates the ionization). Then the recombinations in the shadowed region, Δy, must balance the diffuse incident flux, F_y. Let n_{et} be the electron density in the ionized portion of the shadowed cylinder. Then

$$\alpha_r n_{et}^2 \Delta y \sim \tfrac{1}{12}\alpha_r n_{ea}^2 y_{II}. \tag{30}$$

Roughly, $n_{et} \simeq n_{ew}(r_w/x)^2$, where n_{ew} is the electron density at r_w. In addition, $(1/3)\alpha_r n_{ew}^2 r_w$ is of order $f_r\Phi_i/(4\pi d^2)$ (incident flux equals recombination rate per unit column in ionized flow). Furthermore, the Strömgren condition and the assumption that $y_{II} \sim d_s$, where d_s ($\sim 10^{18}$ cm) is the Strömgren radius in the Orion H II region, gives the relation

$$\alpha_r n_{ea}^2 y_{II} \sim \frac{f_r\Phi_i}{4/3\pi d_s^2}. \tag{31}$$

Therefore,

$$\Delta y \simeq \left(\frac{1}{12}\frac{d^2}{d_s^2}\frac{x^3}{r_w^3}\right)x. \tag{32}$$

The tail ends (merges) at $x = x_t$ when $\Delta y = r_w$, or at

$$x_t \simeq 12^{1/4}\left(\frac{d_s}{d}\right)^{1/2}r_w. \tag{33}$$

Since $d \sim (0.1–0.5)d_s$, the ratio of the tail length to the bow radius, x_t/r_w, is of order 3–6, weakly dependent on d, the distance to θ^1 Ori C. These results correspond with the observations of the shapes of the tails.

In this interpretation, the tail is entirely due to the effect of the diffuse EUV radiation field on the diverging (diffuse FUV-driven) photoevaporative flow from the backside of the disk. This provides a simple explanation for the shapes of the observed tails and does not require flows of material passing from the front hemisphere to the back by the action of winds or radiation pressure.

2.6. Evolution and Structure of the Disk

A great deal of information about the disk systems can be acquired assuming that these circumstellar disks follow the expected power-law models used in accretion disk theories and solar nebula models. In particular, the surface density in the disk varies as a power, $-\alpha$, of the radius,

$$\Sigma(r) = \Sigma_0\left(\frac{r}{r_0}\right)^{-\alpha}, \tag{34}$$

where Σ_0 is the surface density at the fixed location r_0. If $\alpha > 0$ and the disk material does not migrate, then as evaporation of the disk surface proceeds, the outer disk will evaporate before the inner region. Over time the disk will shrink and, following either equation (6) or equation (20), the *total* evaporation rate will also decrease, although the evaporation rate *per unit area* increases. If $\alpha < 2$, most of the disk mass resides near its outer edge, and knowledge of the evaporation rate, evaporation timescale, and current disk size provide the means to determine the current surface density at the outer disk radius and the present disk mass. Comparing the surface densities measured at the outer radius for an ensemble of disks with a range of sizes, we obtain a measure of α (§ 3.3). Standard disk profiles often assume $\alpha = 3/2$, and our procedure described below obtains $1 < \alpha < 3/2$, which satisfies both of the above constraints.

We have shown that the total mass-loss rate from the disk scales as the disk size, $\dot{M}_d \propto r_d^\beta$, where $\beta = 3/2$ for EUV-dominated flows and $\beta = 1$ for FUV-dominated flows. The rate of change of surface density at any instant is constant across the disk (at least between r_g and r_d), and therefore $\dot{\Sigma} \propto r_d^{\beta-2}$. For $\alpha > 0$, there is initially less surface density at large radii, so the disk radius decreases with time, and $\dot{\Sigma}$ increases with time for $\beta < 2$. Therefore, the surface density lost in a time t_i is given approximately as $\Delta\Sigma \simeq \dot{\Sigma}t_i$, where $\dot{\Sigma}$ is the *current* value at time t_i. The current disk size, r_d, is given as the place where the surface density lost over time, t_i, is equal to the original surface density at r_d, $\Sigma(r_d)$:

$$\Sigma(r_d) \simeq \left(\frac{\dot{M}_d}{\pi r_d^2}\right)t_i. \tag{35}$$

A more exact integration of the time history of $\dot{\Sigma}$ at r_d gives the following solution for $\alpha + \beta > 2$:

$$\Sigma(r_d) = \left(\frac{\alpha + \beta - 2}{\alpha}\right)\left(\frac{\dot{M}_d}{\pi r_d^2}\right)t_i. \tag{36}$$

The equation breaks down for $\alpha + \beta < 2$ because the initially infinite-sized (and mass) disk evolves too slowly in size for $t < t_i$; in this case, a finite initial disk size is required for a solution.

For $\alpha > 0$, the surface density inside of r_d has not been strongly affected at $t \lesssim t_i$. The current surface density of the disk as a function of position is just the initial surface density minus the initial surface density at the present disk edge. Therefore, the current mass of the disk is approximately the original disk mass out to r_d, corrected for erosion, or

$$M_d \simeq \left(\frac{\alpha}{2 - \alpha}\right)\pi r_d^2 \Sigma(r_d) \tag{37}$$

for $\alpha < 2$. For $\beta \sim 1–1.5$, $\alpha \sim 1–2$, and $\alpha + \beta > 2$, equations (36) and (37) show that a good estimate of $\Sigma(r_d)$ and M_d can be made, independent of precise knowledge of α and β, if we

know $\dot{M}_d$ (the current mass-loss rate) and t_i. $\dot{M}_d$ is known both observationally and from our theoretical models. As discussed earlier, observations constrain $t_i \sim 10^5$ yr (to a likely uncertainty of a factor of 3). Therefore, we can estimate surface densities at r_d to a factor of order 3, with the largest uncertainty caused by t_i.

Substituting for the disk mass-loss rates determined in §§ 2.2 and 2.3, the surface density at disk edge and the present disk mass may be determined. Setting $t_{i5} = t_i/10^5$ yr, FUV-dominated flows ($\beta = 1$) yield

$$\Sigma(r_d) = 83\left(\frac{\alpha - 1}{\alpha}\right)\epsilon r_{d14}^{-1} t_{i5} \text{ g cm}^{-2} \qquad (38)$$

and

$$M_d \simeq 1.3 \times 10^{-3}\left(\frac{\alpha - 1}{2 - \alpha}\right)\epsilon r_{d14}\, t_{i5}\, M_\odot\,, \qquad (39)$$

assuming $\alpha > 1$. For EUV-dominated flows ($\beta = 3/2$),

$$\Sigma(r_d) = 60\left(\frac{\alpha - 0.5}{\alpha}\right)f_r^{1/2}\Phi_{49}^{1/2}\, d_{17}^{-1} r_{d14}^{-1/2} t_{i5} \text{ g cm}^{-2} \qquad (40)$$

and

$$M_d \simeq 9.5 \times 10^{-4}\left(\frac{2\alpha - 1}{4 - 2\alpha}\right)f_r^{1/2}\Phi_{49}^{1/2}\, d_{17}^{-1} r_{d14}^{3/2}\, t_{i5}\, M_\odot\,, \qquad (41)$$

assuming $\alpha > \frac{1}{2}$.

The evolution of $\dot{M}_d$, the disk size, and the disk mass may also be examined for $\alpha + \beta > 2$. For $\alpha < 2$, the mass in a disk of size $r_d(t)$ scales as $M_d \propto r_d(t)^{2 - \alpha}$. Using this and $\dot{M}_d \propto r_d(t)^\beta$, we obtain at fixed d

$$M_d \propto t^{-(2 - \alpha)/(\alpha + \beta - 2)}\,, \qquad (42)$$

$$\dot{M}_d \propto t^{-\beta/(\alpha + \beta - 2)}\,, \qquad (43)$$

$$r_d(t) \propto t^{-1/(\alpha + \beta - 2)}\,. \qquad (44)$$

For $\alpha = 3/2$ and FUV-dominated flows ($\beta = 1$), $r_d(t) \propto t^{-2}$, $M_d \propto t^{-1}$, and $\dot{M}_d \propto t^{-2}$. For $\alpha = 3/2$ and EUV-dominated flows ($\beta = 3/2$), $r_d(t) \propto t^{-1}$, $M_d \propto t^{-1/2}$, and $\dot{M}_d \propto t^{-3/2}$. When the Trapezium system was only 10% of its present age, the disks were 3–10 times more massive and 10–100 times larger in radius if $\alpha = 3/2$ over this radial range. Although the use of a power-law surface density with $\alpha = 3/2$ requires an infinite mass and extent at the origin of time, the above relation results in small, minimum solar nebula mass disks over most of the lifetime of the Trapezium cluster. If the initial disk had a power-law surface density out to an initial cutoff radius r_{di}, then the equations above hold for times such that $r_d < r_{di}$. These equations also predict the evolution of disks that originate in FUV-dominated regions. Initially, $\beta = 1$, and the disk size, r_d, shrinks with t^{-2} ($\alpha = 3/2$). However, once the disk has shrunk to $r_d \lesssim r_{gI}$, the FUV-dominated flow ceases, and the EUV-dominated flow ($\beta = 3/2$) provides the disk evaporation. Now r_d shrinks with t^{-1} until the disk size drops below $r_d \lesssim r_{gII}$. After this, the photoevaporation effectively ceases in the absence of viscosity. However, viscous timescales for $r_d \lesssim r_{gII}$ can be relatively short compared to t_i (Hartmann et al. 1998) so that the inner disk can rapidly

accrete onto the central star and simultaneously spread beyond r_{gII} to be photoevaporated.

Equations (38)–(44) apply to individual disks with surface densities given by equation (34) at distance d from the ultraviolet source. What relations hold for an *ensemble* of disks at various distances, d, that have all been exposed to ultraviolet radiation for the same time, t_i? In the FUV-dominated region, if all the disks had the same Σ_0 and the same α (> 1), then they would all evaporate to the same size, r_d, at $t = t_i$, regardless of their distance, d, to the UV source, and they would all have the same surface density, $\Sigma(r_d)$. On the other hand, if they all had the same α but a distribution of Σ_0, then those with the higher Σ_0 would be larger at a given instant t_i, with $r_d \propto \Sigma_0^{1/(\alpha - 1)}$ (derived by equating eq. [34] to eq. [38]). The result is a distribution of disks with $\Sigma(r_d) \propto r_d^{-1}$, as derived in equation (38). No constraints on α could be obtained from a measurement of $\Sigma(r_d)$ versus r_d for an ensemble of disk in the FUV-dominated region.

On the other hand, consider the situation in the EUV-dominated region if all the disks had the same α ($> \frac{1}{2}$) and Σ_0. In this region, the evaporation rate depends on d ($\dot{M}_d \propto d^{-1}$, see eq. [23]), so that the disks closer to the UV source will evaporate to smaller sizes after a given time, t_i. In this case, the disk size after a given time is proportional to $d^{2/(2\alpha - 1)}$. Such an ensemble would then show a clear relationship between r_d and d, and the ensemble would present $\Sigma(r_d) \propto r_d^{-\alpha}$. In this case, α can be determined from the observations of disks in the EUV region. Unfortunately, the ensemble of disk would presumably have a distribution of values of Σ_0 instead of a unique value. This produces a biased scatter in a plot of $\Sigma(r_d)$ versus r_d. After a time t_i, the low Σ_0 disks have been preferentially evaporated to small sizes, which flattens the slope of the observed $\Sigma(r_d)$ versus r_d distribution. In § 3.3, we plot $\Sigma(r_d)$ versus r_d for the disks observed in the EUV-dominated region in Orion and derive $\alpha \sim 1$–1.5 for these disks.

McCaughrean & O'Dell (1996) discuss the sharp truncation at the disk edge. We note that the external photoevaporation model discussed above will quickly evolve power-law density distributions into sharply truncated disks.

2.7. Complications

In the above sections, we have concentrated on the interaction of radiation with circumstellar disks. This treatment has ignored the role of the radiation pressure acting on dust and the impact of stellar winds from the Trapezium stars.

Dust entrained in the evaporating gas from the disk readily absorbs ultraviolet photons from θ^1 Ori C. The radiation pressure imparts momentum that opposes the flow powered by the photoheated pressure gradient. Assuming that the gas is completely coupled to the dust, radiation pressure introduces a drag,

$$\Delta\left(v\frac{dv}{dr}\,G\right) = -\frac{L_* \sigma}{4\pi d^2 cm_I}\,, \qquad (45)$$

where v is the velocity of the flow, $L_* \sim 10^{39}$ ergs s^{-1} is the luminosity of the illuminating star, σ is the cross section per hydrogen nucleus for extinction of ultraviolet photons by dust, and c is the speed of light. The stopping distance for perfectly coupled gas and dust, found by substituting $v \sim a_I$, $dv/dr \sim a_I/r_D$, where r_D is the stopping distance from the disk surface, and solving equation (45), is given by

$$r_D \sim 10^{15}d_{17}^2 \text{ cm}\,. \qquad (46)$$

For $d < 10^{17}$ cm, radiation pressure on dust becomes important since the stopping distance is similar to the ionization front radius, $r_D \sim r_{IF}$. However, for photoionized gas, the velocity of interest is $v \sim a_{II}$, which results in a much larger stopping distance. Therefore, once the neutral flow reaches the ionization front, radiation pressure can be ignored. Radiation pressure on grains may influence the appearance and properties of the evaporating sources lying within a projected radius of about $10''$ ($d_{\perp} \lesssim 10^{17}$ cm) of θ^1 Ori C.

This simple treatment ignores several important processes. First, the photoablation flow diverges, so there is an outward pressure gradient which can produce a significant force in the flow direction once it becomes supersonic (see the Parker wind problem: Parker 1963; Shu 1991). Second, in § 3, comparison with HST 182−413 yields $\epsilon \sim 3$. It is possible that part of the high value for ϵ is due to an overestimate of the cross section for extinction by dust, σ, and that dust is depleted or coagulated in the neutral flow. Finally, there may not be complete gas-dust coupling, in which case dust may be pushed back and around the disk.

As discussed in Paper I, there is evidence that the [O III] arcs found several arcseconds from evaporating sources lying within $30''$ of θ^1 Ori C trace the regions in which the fully ionized outflow from the evaporating source interacts with the stellar wind from the massive star. Henney et al. (1996) describe an interacting wind model that may explain these arcs.

Though these effects are expected to contribute to the large-scale appearance of the ionized gas flows that surround an evaporating source, they are not likely to impact in any significant way the appearance of the region lying within the radius of the ionization front facing θ^1 Ori C. Therefore, we omit these effects and concentrate the analysis on evaporating regions close to the disk ($r \lesssim r_{IF}$) where our model is expected to apply.

3. COMPARISON WITH OBSERVATIONS

The above theoretical formulation presents a general model that can be applied to the external evaporation of disks in the Trapezium region of Orion. In this section we compare the model results with observations obtained with HST. The star-disk system HST 182−413 (HST 10) is used to calibrate parameters of the theoretical model, and the ensemble of extended emission objects found in the Trapezium are used to determine estimated disk quantities.

3.1. Hubble Space Telescope Data Acquisition

The HST observations used in this paper are fully discussed in Paper I. Paper I presents the cycle 4 HST data, including a list of objects on the Planetary Camera and Wide Field Camera frames, a table of their observed properties, a discussion of the ionization structure and model fitting of the radial intensity profile of the ionized gas, a detailed discussion of the [O III] arcs, the properties of the tails, and observations of [O I] emission from the silhouettes embedded inside the bright ionized star-disk systems.

Paper I lists several observable properties of about 50 evaporating sources observed with the Planetary Camera (PC) portion of the Wide Field Planetary Camera 2 (WFPC2) on HST or well resolved on wide-field (WF) camera images. The measured parameters include the projected standoff position of the ionization front from the

central star or disk, the width of the ionization front (both measured in Hα and [O III]), the size of the disk (as seen in [O I] emission or absorption in [O III]) if measurable, the standoff distance of the [O III] arc if measurable, and the length and width of the tail (measured in [N II] or [S II]). The coordinates of the central stars in each object were determined from the pixel coordinates using IRAF's STSDAS/METRIC command. We computed the projected radial distance and the physical distance (assuming a distance of 460 pc) between each source and θ^1 Ori C. Tables 1 and 2 list the relevant results. The system names are taken from O'Dell & Wen (1994) except for two Wide Field Camera systems for which the names are placed in parenthesis and come from Prosser et al. (1994). The tables show the projected (perpendicular) distance from θ^1 Ori C to each star-disk system, $d_{\perp}$, the ionization front standoff distance, r_{IF}, and the ionization front width, r_w. Also listed are the disk parameters r_d, $\Sigma(r_d)$, $\Sigma(1\ AU)$, and M_d determined from the numerical model (§ 2.4) using the calibration of HST 182−413 given in the next section. $\Sigma(1\ AU)$ and M_d assume $\alpha = 3/2$, with $\Sigma(1\ AU)$ much more sensitive to the exact value of α.

3.2. Calibration with HST 182−413 (HST 10)

We use observations of HST 182−413, one of the largest and best observed star-disk systems with an extended ionized envelope, to calibrate the parameters of the model presented in § 2. In this system, which is nearly $2''$ in extent, both the ionization front and the disk are clearly seen and well resolved.

Our images of HST 182−413 have an angular resolution of $0''.046$, or more than a factor of 2 better than the images presented by McCaughrean & O'Dell (1996). In our PC images of HST 182−413 (Fig. 8), the ionization front is teardrop-shaped and roughly centered on an opaque and nearly edge-on disk seen in silhouette. The edge-on disk completely obscures the central star, even at wavelengths as long as 3.8 μm (M. J. McCaughrean 1997, private communication), which implies that the visual extinction to the star is at least 50–100 mag or that $N(H) \gtrsim 10^{23}$ cm^{-2} for a normal gas-to-dust ratio. The silhouette is resolved along its minor axis over its entire length, which indicates that it is a thick disk with a minor axis full width of about 0.2 times the radius.

The ionization front is well separated from the disk, permitting a good determination of the IF standoff distance. Its shape, however, is not symmetric about a line connecting HST 182−413 to θ^1 Ori C. The teardrop's major axis is aligned with the minor axis of the edge-on disk. The Hα surface brightness of the ionization front does reach its greatest value on the side of the object directly facing the Trapezium.

Though the disk is visible as a silhouette in the continuum, in Hα, in [N II], in [S II], and in [O III], the $\lambda = 6300$ Å [O I] image shows the disk in emission. Furthermore, the disk is bright in the 2.1218 μm $S(1)$ line of H_2 (Bally, Latter, & Devine 1998b; Chen et al. 1998). H_2 emission was first detected from the ground by means of high-dispersion spectroscopy that permitted the YSO emission to be distinguished from the fluorescent background that permeates the Orion Nebula. Chen et al. used the near-infrared camera and multiobject spectrometer (NICMOS) on HST to demonstrate that all of this emission is produced by the disk. The silhouette, [O I], and H_2 emission coincide to

TABLE 1

PARAMETERS FOR TRAPEZIUM STAR-DISK SYSTEMS: PLANETARY CAMERA

System	d (10^{17} cm)	$r_{\rm IF}$ (10^{17} cm)	r_w (10^{17} cm)	r_d (10^{17} cm)	$\dot{M}$ (10^{-7} $M_\odot$ yr^{-1})	$\Sigma(r_d)$ (g cm^{-2})	Σ(1 AU) (g cm^{-2})	M_d ($M_\odot$)
163−323	0.14	<3.1	3.1	2.2	2.51	106	6100	0.025
161−324	0.41	<3.1	3.1	2.0	0.86	46	2200	0.009
168−326	0.44	<3.1	6.2	4.1	2.24	28	4000	0.023
168−328	0.46	<3.1	3.1	1.9	0.77	43	2000	0.007
163−317	0.47	8.4	6.2	4.1	2.13	27	3900	0.021
166−316	0.49	<3.1	3.1	1.9	0.72	42	1900	0.007
161−328	0.51	<3.1	7.8	5.1	2.75	22	4400	0.028
167−317	0.53	4.7	7.8	5.1	2.64	22	4300	0.026
158−323	0.63	4.7	4.7	2.8	1.03	28	2200	0.010
158−326	0.64	12.7	12.1	7.9	4.21	14	5500	0.042
158−327	0.71	11.5	17.1	11.3	6.34	10	6900	0.064
157−323	0.74	<3.1	3.1	1.7	0.48	34	1300	0.005
170−337	1.09	11.5	14.3	8.5	3.18	9	4000	0.042
176−325	1.11	4.7	5.7	2.9	0.80	20	1700	0.032
169−338	1.11	<3.1	3.9	1.9	0.44	27	1200	0.005
154−324	1.11	<3.1	3.1	1.5	0.32	31	900	0.003
159−338	1.19	9.3	6.2	3.1	0.84	18	1700	0.008
171−340	1.28	12.7	12.9	7.2	2.31	10	3200	0.023
152−319	1.29	11.5	9.3	4.9	1.42	13	2400	0.014
155−338	1.40	15.2	15.7	8.7	2.85	8	3500	0.029
173−341	1.52	6.2	7.1	3.2	0.81	16	1600	0.008
	1.53	<3.1	5.4	2.3	0.53	21	1300	0.005
180−331	1.67	12.1	12.9	6.3	1.78	9	2600	0.018
177−341	1.72	23.0	23.6	13.0	4.27	5	4300	0.043
159−350	1.92	19.9	20.0	10.1	3.00	6	3400	0.030
175−355	2.42	6.2	7.8	2.4	0.57	20	1300	0.006
	2.56	<3.1	4.7	1.3	0.25	30	800	0.002
174−414	3.56	9.3	7.8	1.2	0.39	61	1300	0.004
182−413	3.85	62.7	39.3	12.3	4.11	6	4300	0.041
184−427	4.71	6.2	7.9	0.9	0.30	79	1200	0.003

within 0.05″ (25 AU). Fluorescence or FUV pumping is the most likely excitation for the H_2 emission. If this interpretation is correct, then the H_2 observations provide direct evidence that FUV photons penetrate to the disk surface. The presence of [O I] emission also indirectly implies the presence of a strong FUV radiation field in the emission region to supply the energy necessary to excite this line which lies 2 eV above ground.

Unlike H_2, [O I] emission is also seen from the vicinity of the IF and from the interior of the neutral envelope. The emission near the IF is easily explained by electron impact excitation at the base of the EUV ionized flow since the ionization potential of O I is 13.6 eV, identical to that of hydrogen. The distributed [O I] emission in the neutral envelope above the disk may indicate the presence of a bipolar outflow from the embedded YSO which might collisionally excite the [O I] emission in this region. A YSO

wind may explain the elongation of the IF along an axis orthogonal to the disk (note $r_{\rm IF} > r_w$ in Table 1) but cannot explain the [O I] or H_2 emission from the disk surface. Despite the possible effects of a collimated wind along the disk minor axis, we can use this source as a calibration by using r_w, the ionization front width, to estimate $r_{\rm IF}$. We use r_w to measure $r_{\rm IF}$ in all of the systems. This measurement is easier to perform because of the (generally) slightly larger size of the width versus standoff distance and because it depends less on the actual placement of the embedded source.

The ionization front width in HST 182−413 is measured to be $r_w = 3.9 \times 10^{15}$ cm, and the disk radius is $r_d = 1.3 \times 10^{15}$ cm. The projected distance separating HST 182−413 from θ^1 Ori C is $d_\perp = 3.8 \times 10^{17}$ cm. Using this distance as a measure of the separation between the stars introduces an underestimate in d with an uncertainty of

TABLE 2

PARAMETERS FOR TRAPEZIUM STAR-DISK SYSTEMS: WIDE FIELD CAMERA

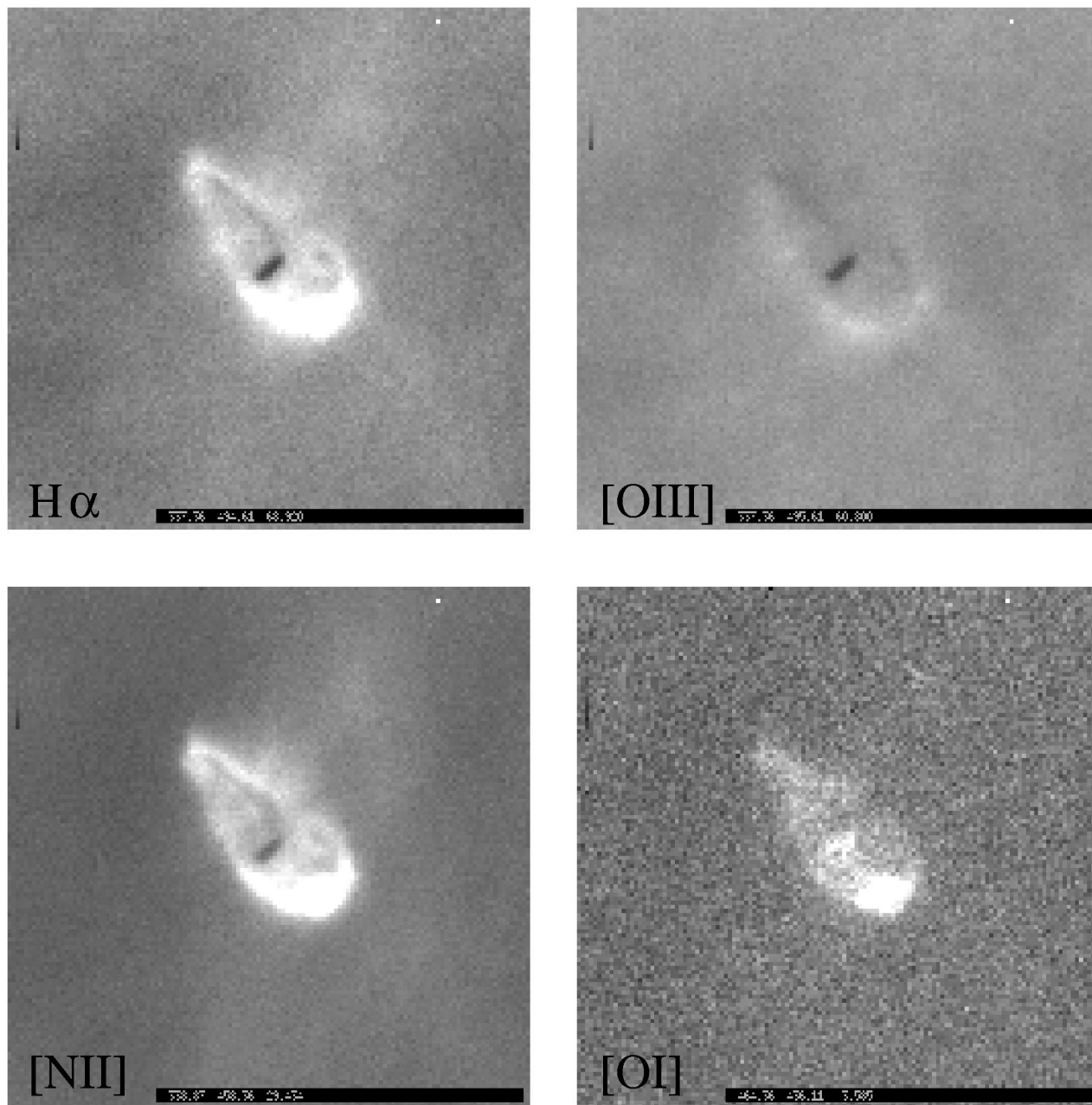| System	d (10^{17} cm)	$r_{\rm IF}$ (10^{17} cm)	r_w (10^{17} cm)	r_d (10^{17} cm)	$\dot{M}$ (10^{-7} $M_\odot$ yr^{-1})	$\Sigma(r_d)$ (g cm^{-2})	Σ(1 AU) (g cm^{-2})	M_d ($M_\odot$)
(69)	2.74	<6.7	23.7	10.0	2.70	6	3100	0.027
	3.08	<6.7	24.7	9.4	2.56	6	3000	0.026
	3.30	12.0	20.0	4.2	1.75	21	3100	0.017
159−418	3.74	<6.7	13.4	1.8	0.84	54	2300	0.008
	5.15	13.4	17.0	1.6	0.88	69	2500	0.009
(7)	5.18	20.0	18.4	1.8	0.98	64	2700	0.009
	5.59	13.4	20.0	1.8	1.03	65	2800	0.010
138−207	5.76	36.8	43.1	5.5	3.15	22	4900	0.032
	8.27	20.0	12.4	0.8	0.34	101	1300	0.004
157−533	8.80	36.8	27.7	1.7	1.07	77	3000	0.009
	9.47	24.7	20.0	1.1	0.61	98	2100	0.006

FIG. 8.—*HST* images of HST 182−413 in four filters. Clockwise from the top left are Hα, [O III], [O I], and [N II]. Note that the disk appears in absorption for all filters except [O I] and that the ionization front, seen most clearly in Hα and [O III], is offset from the disk surface.

order $\delta d/d \sim 4/(\pi - 1) \sim 0.3$ in the following analysis. Comparison of the observed values of r_d, r_{IF}, and d with the analytic equations presented in § 2.3 (e.g., eq. [10]) or the numerical models described in § 2.4 results in an empirical calibration of the parameter $\epsilon/(f_r \Phi_{49})^{1/2}$:

$$\epsilon/(f_r \Phi_{49})^{1/2} = 4 . \qquad (47)$$

Separating these parameters proves difficult and model dependent. The literature (Churchwell et al. 1987; Garay et al. 1987) contains numerous claims that θ^1 Ori C produces more Lyman continuum photons than are used in balancing recombination in the ionized envelopes, presumably because ionized photons are lost due to dust absorption or leak out of the H II region along lines of sight with low density. However, for the present purpose it is acceptable to assume that $f_r \Phi_{49} \sim 0.5$ (recall $1 - f_r$ is the fraction of EUV

absorbed by dust), and $\epsilon \sim 3$. Since $f_r \Phi_{49}$ enters only as a square root, ϵ is unlikely to be significantly underestimated.

Further examination may find that $\epsilon/(f_r \Phi_{49})^{1/2}$ is not entirely independent of each unique evaporating disk system, and therefore a single value may not be appropriate. However, using the above calibration for HST 182−413, the model disk sizes have been computed for the 15 systems with observable bright [O I] disks found in Paper I. While the match is not perfect, Table 3 shows that there is a strong correlation between observed disk size and computed model disk size and that the absolute sizes of the model disks are comparable to the observed [O I] disk sizes. Only two of the 15 sources show real disagreement (HST 158-327 and HST 175-355). Therefore, the calibration (eq. [47]) derived for HST 182−413 is valid for most of the sources where both r_d and r_{IF} are measured.

TABLE 3
OBSERVED VERSUS MODELED DISK SIZE

System	d (10^{17} cm)	Observed r_d (10^{14} cm)	Modeled r_d (10^{14} cm)
166−316......	0.49	∼3.1	1.9
161−328......	0.51	6.1	5.1
158−326......	0.64	6.1	7.9
158−327......	0.71	3.1	11.3
170−337......	1.09	6.1	8.5
159−338......	1.19	∼3.1	3.1
171−340......	1.28	6.1	7.2
152−319......	1.29	6.1	4.9
155−338......	1.40	6.1	8.7
173−341......	1.52	∼3.1	3.2
177−341......	1.72	∼12.2	13.0
159−350......	1.92	6.8	10.1
175−355......	2.42	6.1	2.4
182−413......	3.85	12.3	12.3
184−427......	4.71	∼3.1	0.9

Using $\epsilon = 3$ as the coefficient for the warm, evaporative flow yields a quantitative analysis of the evaporating HST 182−413 star-disk system. The mass-loss rate is found using the theory of § 2.2 and the numerical model described in § 2.4, yielding

$$\dot{M} = 4.1 \times 10^{-7} \, M_\odot \, \text{yr}^{-1} \qquad (48)$$

and assuming a standard disk structure ($\alpha = 3/2$) and ionization lifetime $t_i = 0.1$ Myr ($t_{i5} = 1$), the surface density at the disk edge is $\Sigma(r_d) = 6t_{i5}$ g cm^{-2}. This converts to a present-day disk mass of $M_d = 0.041t_{i5} \, M_\odot$. These results depend only weakly on α for $1 < \alpha < 2$ (see eqs. [38] and [39]). Computing the surface density at 1 AU, taking $\alpha = 3/2$, produces $\Sigma(1 \text{ AU}) = 4.3 \times 10^3 t_{i5}$ g cm^{-2}. These results indicate that the disk surrounding HST 182−413 is similar to the hypothesized minimum solar nebula disk, a result that will be discussed further in § 3.4.

3.3. Application to the Ensemble of Evaporating Disks

In this section, we apply the calibration of HST 182−413 to the entire ensemble of evaporating disks. We use measurements of the ionization front standoff distance and the distance from θ^1 Ori C to estimate the disk size, surface density, mass, and mass-loss rate. Given that the mass lost from the disk must escape from the gravitational potential of the embedded star, disks with $r_d \lesssim 0.5 r_{gI}$ should not produce significant neutral evaporation. From the discussion in § 2, the minimum size for an FUV-dominated evaporating disk should be of order $r_d \sim 10^{14}$ cm. Any system with an ionization front size $r_{IF} \lesssim 10^{14}$ cm will *not* produce a significant separation between disk and IF. Smaller disks might have EUV-dominated evaporation, but then the dominant emission will come from close to the disk surface. Since an *HST* PC pixel subtends 21 AU, sources having disk dimensions close to this critical value will be unresolved, making a direct determination of the cutoff size for neutral evaporation (and separation of disk from IF) difficult.

While observations of systems with small circumstellar disks are difficult when the disk reaches $r_d \sim 10^{14}$ cm, large disks and their offset ionization fronts should be clearly visible in the *HST* images. However, if there exists a maximum value for the initial surface density coefficient, Σ_0 (see § 2.6), then at any distance from θ^1 Ori C, a maximum current (remnant) disk size should be found. Using 6 times

the minimum solar nebula limit (Hayashi et al. 1985), $\Sigma(1 \text{ AU}) = 6000$ g cm^{-2}, and assuming $\alpha = 3/2$, the largest remnant disks remaining after $t_i = 10^5$ yr were computed at all distances from θ^1 Ori C. In the following discussion, we show that the ensemble of star-disk systems observed in Orion's Trapezium can be explained by a range of initial disk surface densities bounded above by $\Sigma(1 \text{ AU}) \sim 6000$ g cm^{-2}.

Figure 9 plots the ionization standoff radius, r_{IF}, versus distance from θ^1 Ori C for the ensemble of evaporating star-disk systems in the Trapezium. Objects whose standoff distance is larger than 1 pixel are denoted by stars, while those with an unresolved standoff distance are plotted as plus signs. For reference, HST 182−413 is enclosed in a diamond. Note that the separation distance, d, used in the plot is the measured perpendicular distance between sources and thus underestimates the actual separation by ignoring depth effects. This is likely to introduce an error, $\delta d/d \sim 0.3$, which moves each source slightly to the right in the figures.

In order to compare the *HST* observations with the theory discussed in § 2, a set of model runs were computed following § 2.4, and the curves are placed over the ensemble data points. The solid lines represent the predicted ionization front offset with distance from θ^1 Ori C for disks with radii 10^{14}, 2×10^{14}, 5×10^{14}, 10^{15}, and 2×10^{15} cm, where we have numerically solved for the combined effect of FUV and EUV incident fluxes. When the separation between θ^1 Ori C and the star-disk system is small ($d \lesssim 10^{17}$ cm), the ionization front reaches to the disk surface, producing the horizontal limits seen for curves on the left edge in Figure 9 ($r_{IF} = r_d$). This relation follows from equation (22); the effective pressure of the ionized gas at the IF pushes the neutral region into a thin, dense layer. With growing distance, the ionization front moves away from the disk, a result that is more evident for smaller disks. Eventually, at $d \gtrsim 3 \times 10^{17}$ cm, the neutral layer becomes a neutral wind, and the mass-
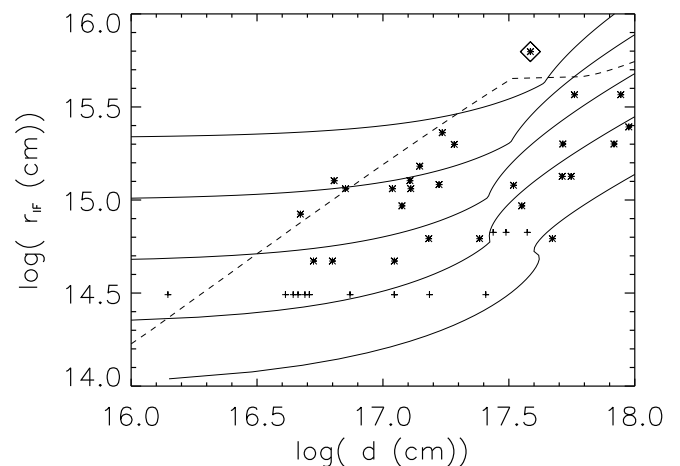

FIG. 9.—For each of the 40 sources measured from the *HST* images, the distance from θ^1 Ori C is plotted vs. the standoff distance of the ionization front (both measured in centimeters). The stars represent measured values, while the plus signs represent upper limits. HST 182−413 is enclosed in a diamond for reference. The five solid lines denote the expected relation for evaporating systems with disks of size 10^{14}, 2×10^{14}, 5×10^{14}, 10^{15}, and 2×10^{15} cm, respectively (*bottom to top*). The dashed line indicates the maximum ionization front offset at any radius, assuming that the surface density profile for the initial disks did not exceed 6 times the minimum solar mass limit (see text).

loss rate becomes independent of distance. Kinks occur in the numerical results when the neutral layer grows large enough to support a supersonic disk wind, but the column density is dominated within the shocked layer between the neutral wind and the IF. Beyond this distance, the ionization front varies with $r_{\rm IF} \propto d^{2/3}$, producing the upward turn for the curves on the right edge of Figure 9. This relation follows directly from the analytic result (eq. [10]) for the position of the IF given a constant mass-loss wind.

The dashed line in Figure 9 indicates the position of the ionization front for a maximum surface density disk that has been evaporating for $t_i \sim 10^5$ yr. This truncation curve provides a reasonable upper envelope for the data points, while the curve representing $r_d = 10^{14}$ cm provides a reasonable lower threshold at large distances. At small distances from θ^1 Ori C, these small disks have ionization fronts that are unresolved in either standoff distance or width. We terminate the figure at $d \gtrsim 10^{18}$ cm, since the FUV flux becomes too small to heat the PDR gas significantly beyond this distance.

Figure 10 shows the same analysis determined for the ionization front width, where the relation $r_w = 1.3\ r_{\rm IF}$ (eq. [28]) has been used. Given that the ionization front width is easier to measure than the standoff distance, the remainder of the analysis of the ensemble uses $r_{\rm IF}$ calculated from the measured r_w.

The computed mass-loss rate is plotted in Figure 11 over the grid of constant-sized disks described above. The structure of the evaporating disk models follow closely the analytic theory outlined in §§ 2.2 and 2.3. Close to θ^1 Ori C ($d \lesssim 2.5 \times 10^{17} r_{d14}^{1/2}$ cm), the mass loss is dominated by the EUV photon flux, and for a given disk size, the evaporation rate decreases with distance as d^{-1} (eq. [23]). Kinks occur where the warm neutral layer develops a disk wind and the column is dominated by the shocked layer. In the FUV-dominated region ($2.5 \times 10^{17} r_{d14}^{1/2}$ cm $\lesssim d \lesssim 10^{18}$ cm), the mass-loss rate tends to the fixed value given in the analytic theory (eq. [6]).

Many of the observed sources plotted in Figure 11 fall in the EUV-dominated region near θ^1 Ori C, but a significant number fall in the FUV-dominated region. There appears to be an upper cutoff in the observed mass-loss rate. It is
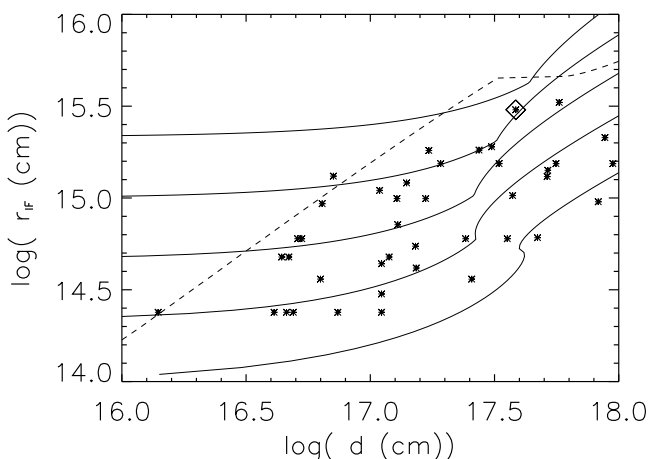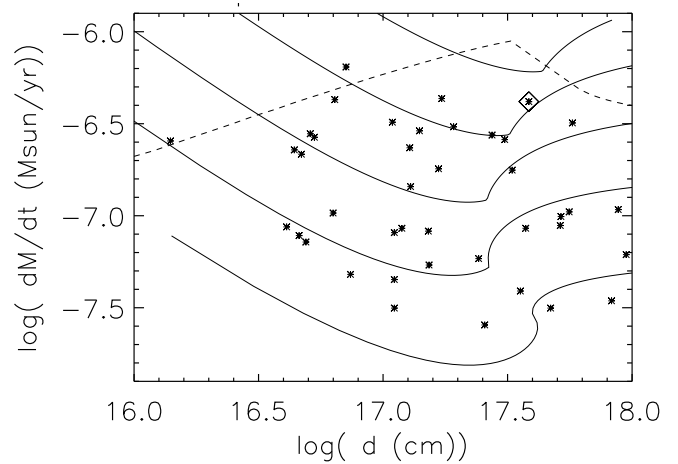

FIG. 11.—Computed mass-loss rate for the ensemble of star-disk systems in the Orion Trapezium. The solid lines represent the mass-loss rates for the disk sizes outlined in Fig. 9 (disk sizes increase from bottom to top). The dashed line denotes the upper envelope of mass loss attained if the initial disks did not exceed 6 times the minimum solar mass surface density.

possible that star-disk systems once existed beyond this upper bound but have already evaporated to smaller sizes and mass-loss rates. This conclusion is reinforced by the dashed upper envelope curve representing the maximum surface density disks evolutionary position after $t_i = 10^5$ yr.

Figure 12 plots the computed disk size for each of the observed systems. Close to θ^1 Ori C, the circumstellar disks appear somewhat smaller than those found at larger distances due to the higher mass-loss rates and hence quicker erosion as predicted in § 2.6. The dashed line plots the radius to which maximum surface density disks would have truncated during $t_i = 10^5$ yr of evaporation. Table 3 pre-
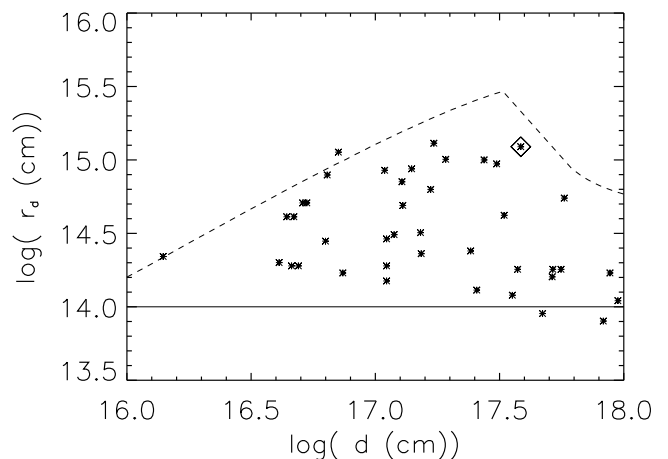

FIG. 12.—Computed disk sizes for the ensemble of star-disk systems in the Orion Trapezium. Note that a significant majority of disks lie between the fiducial values of 10^{14} and 10^{15} cm. The evaporating disk model hypothesizes that erosion truncates the disk and thus produces an evolution downward in the diagram. Disks with radii smaller than a critical radius, $r_d < 0.5 r_{gl} \sim 10^{14}$ cm (see text), are no longer able to evaporate, which perhaps explains the lack of objects observed with small disks. The solid line represents a disk size of 10^{14} cm, while the dashed line represents the maximum disk size observed if erosion has truncated disks with the maximum surface density profile of 6 times the minimum solar mass limit.

FIG. 10.—As in Fig. 9, except the width of the ionization front has been used to determine $r_{\rm IF}$. Note that there is little difference between these two figures.

sents the computed disk sizes versus the 15 observed bright [O I] disk sizes from Paper I for comparison.

Figure 12 and the narrow range of d for FUV-dominated flows presents an explanation for the uniqueness of HST 182−413; only over a limited distance range may large disks with significantly offset ionization fronts exist. That there appear to be no disks with inferred sizes smaller than $\sim 10^{14}$ cm reinforces the notion that FUV-dominated flows are cut off when $r_d \sim 0.5 r_{gI}$. This result is more clearly seen in Figure 10, where the lowest solid line represents model disks with $r_d = 10^{14}$ cm. Within the inner part of the nebula, small disks may not be observed because the IF, coincident with the disk surface, is more compact than the *HST* PC resolution. However, at large distance, the IF expands away from the disk surface and should be easily observed in the *HST* images. The lack of small ionized envelopes at large distance from θ^1 Ori C suggests either that all disks are larger than 10^{14} cm or that disks smaller than this size are inefficient at evaporation. From the results in Paper I, we estimate that the fraction of low-mass stars with extended emission drops from 80% at the cluster center to 50% near the edge. However, for those systems with extended emission, the sample is complete, provided $r_{IF} \gtrsim 3 \times 10^{14}$ cm.

Figure 13 plots the disk sizes versus ionization front offset for the evaporating Trapezium star-disk systems. The solid line signifies ionization fronts located at the disk surface. The dashed line represents the location of the ionization front for maximum surface density disks. HST 182−413 is among the largest disk sources, providing the resolution required to clearly see the silhouette. The ionization front is also well offset from the disk, allowing a clear separation of the two components. While other systems have larger fractional offsets between the disk and the ionization front, none of the other large disks are so well situated. The envelope produced by the maximum surface density evaporation model limits the possible parameter space in which a system like HST 182−413 can exist.

Following the theory set out in § 2.6, Figure 14 presents the surface density at the disk edge versus the size of the

FIG. 14.—Surface density of the circumstellar disks within the EUV-dominated region computed at disk edge using the evolutionary model described in the text. The factor t_{i5} accounts for the uncertainty in the evaporation time and its effect on the surface density (see text). The upper dashed line represents 6 times the minimum solar nebula surface density (slope = −1.5). The lower dashed line represents a slope of −1 for comparison.

disk for disks in the EUV-dominated region. Assuming that all disks have the same power law α, the trend observed in this plot is complicated by the distribution of the initial surface density coefficients, Σ_0, for the disks (see § 2.6). This complication makes determination of an unambiguous α difficult to extract from the figure. However, an upper bound to the data points is well fit by a slope of −3/2 (the upper dashed line represents the location and slope [$\alpha = 3/2$] of a 6 times minimum solar nebula surface density). Also plotted is a line with $\alpha = 1$ for comparison. Only disks that initially had extremely high Σ_0 may be large at the present epoch. As Σ_0 decreases, the maximum-sized disk still existing also decreases. The evolution flattens the slope of $\Sigma(r_d)$ versus r_d of the ensemble by preferentially evaporating low-Σ_0 disks and thereby eliminating disks with low Σ at large r_d (see § 2.6). The bounds of the observations suggests $1 < \alpha \sim 3/2$. For consistency, throughout the rest of this paper we continue to use $\alpha = 1.5$. Comparison with § 2.6 shows that the solution is not strongly dependent on $1 < \alpha < 3/2$. However, it is quite exciting that the observations of this large ensemble, coupled with our model, provide a crude estimate of α.

The surface densities at 1 AU are plotted in Figure 15 assuming $\alpha = 3/2$. Unlike $\Sigma(r_d)$, $\Sigma(1 \text{ AU})$ is sensitive to the choice of α. Only high surface density disks exist near θ^1 Ori C, which reinforces the idea that less massive disks have completely evaporated (or at least have been truncated to their minimum disk radius). The solid line denotes the surface density at 1 AU of disks with $r_d = 10^{14}$ cm that have survived 10^5 yr of evaporation. An approximate upper bound for the surface density is marked by the dashed line, $\Sigma(1 \text{ AU}) = 6000 \text{ g cm}^{-2}$.

Finally, the computed disk masses are presented in Figure 16 along with the minimum disk size model and maximum surface density model described above. All of the disks have low masses, $M_d \lesssim 0.07 t_{i5} \, M_\odot$, and half have masses $M_d < 0.02 t_{i5} \, M_\odot$.

3.4. Circumstellar Disk Masses

A number of nonevaporating, silhouetted disks are observed in the Trapezium region of Orion (O'Dell & Wen
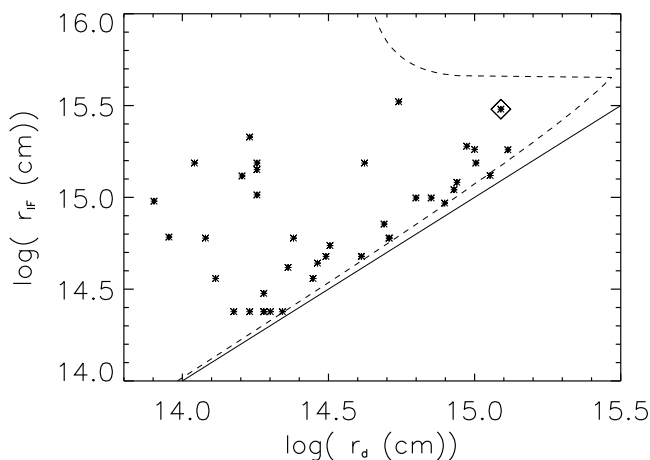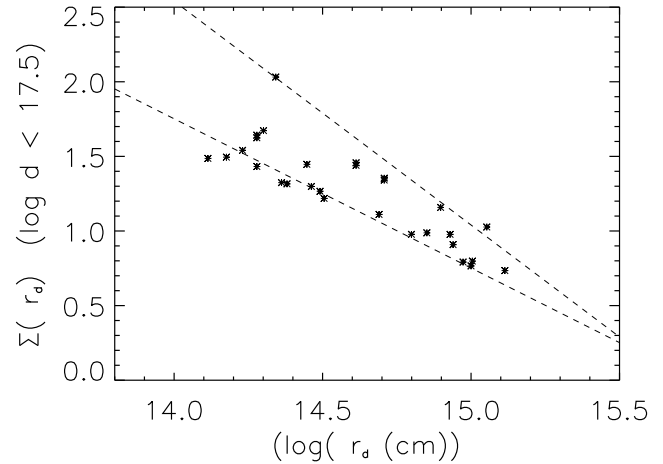

FIG. 13.—Computed disk sizes for the ensemble of star-disk systems in the Orion Trapezium vs. the ionization front offset. The solid line represents ionization fronts located at the disk surface. The dashed line envelops the region with the evolutionary maximum surface density disks assuming no evaporating disks beyond 10^{18} cm. Note that HST 182−413 (*star enclosed in diamond*) has one of the largest disks *and* one of the largest ionization front offsets.
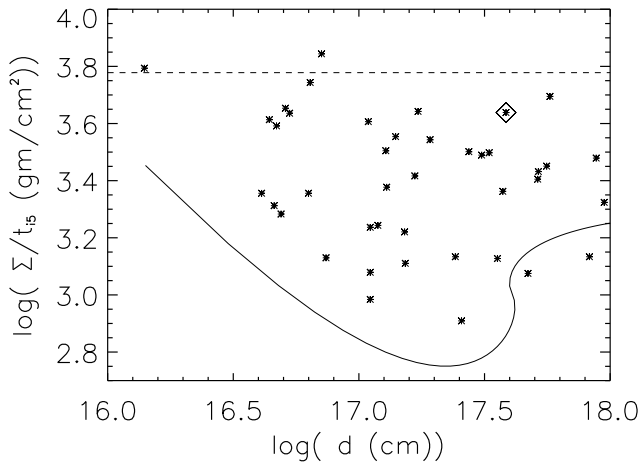
FIG. 15.—Surface density of the circumstellar disks in Orion computed at 1 AU and calculated using the evolutionary disk model described in the text. The factor t_{i5} accounts for the uncertainty in the evaporation time and its effect on the surface density (see text). The surface density for the minimum mass solar nebula is $\Sigma(1 \text{ AU}) \sim 10^3$ g cm^{-3}. The solid line represents the surface density of disks with $r_d = 10^{14}$ cm, disks that have likely almost completed evaporating. The dashed line represents 6 times the minimum solar nebula surface density.

1994; McCaughrean & O'Dell 1996). The directly observed sizes of these disks allow for a comparison between the strongly evaporating disks and these relatively quiescent disks, presumably located farther from θ^1 Ori C or in a region shielded from the EUV flux. The quiescent disks are on average larger than those inferred from the strongly evaporating systems, with radii $r_d \gtrsim 1.5 \times 10^{15}$ cm. Since the average disk size for the strongly evaporating systems is $r_d \sim 3.0 \times 10^{14}$ cm, the hypothesis that evaporation destroys the disk from the outside inward appears reasonable. This hypothesis requires $\alpha > 0$.
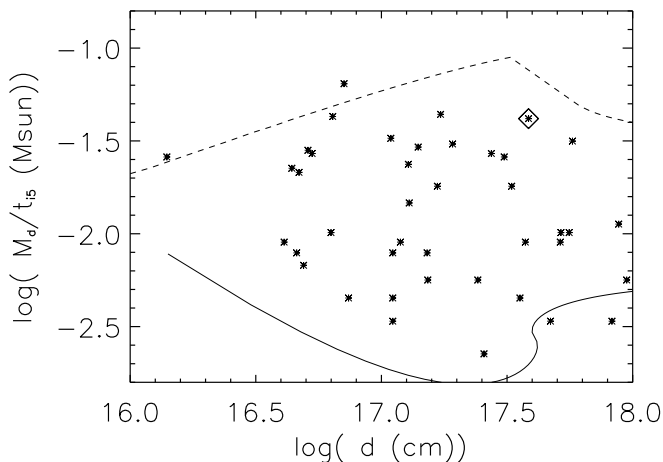

FIG. 16.—Following from Fig. 15, the computed disk mass for the circumstellar disks in the Orion Trapezium. The factor t_{i5} accounts for the uncertainty in the evaporation time and its effect on the disk mass (see text). The computed masses are consistent with the minimum solar nebula disk mass, observations of disk masses around other young stars, and the detailed disk mass observations performed in the Trapezium (see text). The solid line indicates the smallest disk observable and places a lower envelope around the disk masses. The dashed line produces an upper envelope around the points and represents disks that initially had 6 times the minimum solar nebula surface density.

Estimating masses for the silhouetted disks is very complicated, and McCaughrean & O'Dell (1996) only produce lower limits to the disk mass. The silhouettes are not completely dark, possibly suggesting that the optical depth is small through the disk and allowing a mass determination. However, the observed illumination may actually be scattered light from the embedded star, foreground illumination, or an artifact of the *HST* point-spread function. McCaughrean & O'Dell claim that the observations are consistent with "no flux being *transmitted* through the centers of the disk," but they calculate the absolute lower limit to the disk mass using the observed illumination as a measure of minimum optical depth. In all cases, these lower limit masses are much less than the estimated disk masses given in the preceding section. Therefore, we predict that the disks are, in fact, completely opaque.

Direct measurement of the mass in Trapezium circumstellar disks was attempted by Mundy, Looney, & Lada (1995). They concluded that an upper limit to the mass of any disk was $M_d \lesssim 0.15 \ M_\odot$ and that statistically, the disks must have mass $M_d < 0.03 \ M_\odot$. More recent observations by (E. Lada 1997, private communication) have determined disk masses $M_d \sim 0.01 \ M_\odot$ around a few of the evaporating systems. These values appear consistent with millimeter observations of other circumstellar disks performed by Terebey, Chandler, & André (1993), who concluded that the average disk mass should be $M_d \sim 0.02 \ M_\odot$ around class I sources, with very few massive $M_d > 0.5 \ M_\odot$ disks. A search for continuum and ^{13}CO $J = 2$–1 emission at a wavelength of 1.3 mm is underway at the Owens Valley Radio Observatory (Bally, Testi, & Sargent 1998a).

The median disk mass determined in the preceding section is $M_d \sim 0.02 t_{i5} \ M_\odot$, while the spread in disk mass is $0.002 t_{i5} < M_d/M_\odot < 0.07 t_{i5}$. Changing the computed disk masses is most readily accomplished by varying the evaporation time, t_i (eq. [36]), although $\alpha < 1.5$ will also lower the mass estimates somewhat. Our independently derived masses are consistent with the above measurements for $t_i \lesssim 10^5$ yr ($t_{i5} \lesssim 1$).

4. CONCLUSION

In this paper, we have presented a model for the external UV-induced evaporation of clumps or circumstellar disks and applied this model to the extended ionized sources in Orion's Trapezium. Utilizing the energetic radiation from θ^1 Ori C, we present a scenario in which FUV (6–13.6 eV) and EUV photons heat the surfaces of circumstellar disks surrounding the embedded low-mass stars. The FUV heating produces either a thin, slowly flowing neutral layer or a neutral disk wind with a characteristic speed of $(1$–$2)a_I \sim (3$–$6)$ km s^{-1}. The neutral, $T \sim 1000$ K flow penetrates the ionization front at a standoff distance, r_{IF}, determined by ionization-recombination equilibrium in the ionized flow. The ionization front determines the observed size of the extended ionized envelopes.

The model presents a method of probing the evolution of star-disk systems in the Trapezium. After the young low-mass stars were born $\sim 10^6$ yr ago, θ^1 Ori C ionized the region and initiated the external evaporation of the circumstellar disks, apparently $\lesssim 10^5$ yr ago. Through the combined action of EUV and FUV photons, the disks were heated, produced thermal winds, and lost material from their surfaces. The most rapid disk erosion occurs for large systems or ones that are close to the Trapezium. Within

$d \lesssim 10^{17}$ cm of θ^1 Ori C, ionizing radiation reaches the disk surface directly, heats it to 10^4 K, and powers rapid disk erosion. Figures 9 and 10 (see also Fig. 13) show that a few systems with $r_{IF} = r_d$ may still survive. For the range 10^{17} cm $\lesssim 2.5 \times 10^{17} r_{d14}^{1/2}$ cm, the EUV still powers the erosion, but the FUV produces a thick ($\Delta r \sim r_d$) PDR which enhances the mass loss. Farther out in the nebula, at $2.5 \times 10^{17} r_{d14}^{1/2}$ cm $\lesssim d \lesssim 10^{18}$ cm, the ionization front detaches farther from the disk if $r_d \gtrsim r_{gI}$, a neutral wind is created, and mass-loss is powered by FUV photons. Even farther out, the PDR is not sufficiently heated to power neutral winds, and EUV-dominated flow again proceeds, eroding the disk but at a reduced rate because of the weakness of the EUV flux. Photoerosion leads to disk truncation, shifting the objects downward in Figures 9 and 10.

In the FUV-dominated region, the disks will continue to evaporate and shrink until they reach a size at which the heated neutral material is unable to escape from the potential well of the embedded star: $r_d \sim 0.5 r_{gI}$. For a 0.2 $M_\odot$ star, the minimum disk size for an FUV-heated wind is $r_d \lesssim 10^{14}$ cm, with an uncertainty in size due to the thermal pressure gradients in the wind on the flow (see § 2). When the disk reaches the minimum size for an FUV-heated neutral layer of disk wind, the ionization front once again can reach the disk surface. Direct photoionization of the disk will continue the evaporation process, allowing the disk to evolve to the smaller size where $r_d \sim 0.5 r_{gII}$. However, the rate at which the disk erodes will be smaller (see eq. [23]). We have ignored the effect of migrating disk material that might repopulate the disk beyond the truncation radius and lead to further disk erosion.

Assuming that the ionization age of the Trapezium is $t_i \sim 10^5$ yr and that disk structure follows the power-law profile presented in § 2.6 with a maximal surface density coefficient, the truncation of the observed disks will be complete in less than $\sim 10^6$ yr for $d \lesssim 10^{18}$ cm. We predict final disk sizes of $r_d \lesssim 1$ AU, reached about 10^6 yr after the onset of UV illumination of the circumstellar disk. If the disks have even minimal viscosity, the entire disk is evaporated and accreted on this timescale.

Calibrating the model with HST 182−413, a star-disk system with observable disk size r_d, ionization front offset r_{IF}, and distance $d_\perp$ from θ^1 Ori C allows for a determination of the structure of 40 evaporating disks observed in the Trapezium. The calibration is checked against 14 other systems with measured r_d, r_{IF}, and d. Utilizing an evaporation age for the region somewhat younger than the cluster age, $t_i = 10^5$ yr ($t_{i5} = 1$), adopting the standard surface density disk model, $\Sigma(r) \propto r^{-\alpha}$, and using the observed r_{IF} and $d_\perp$ of each system, we determine the evolution of star-disk systems, produce an independent disk mass estimator, and obtain an estimate of the sizes, mass-loss rates, surface

densities, and α of the 40 disks. We find disk masses of $0.002 t_{i5} < M_d/M_\odot < 0.07 t_{i5}$, disk sizes of 10^{14} cm $\lesssim r_d \lesssim 1.5 \times 10^{15}$ cm, and mass-loss rates of $2 \times 10^{-8}\ M_\odot$ yr$^{-1} \lesssim \dot{M} \lesssim 7 \times 10^{-7}\ M_\odot$ yr^{-1}. The surface density at the disk edge, $\Sigma(r_d)$, falls in the range $5 t_{i5}$ g cm$^{-2} \lesssim \Sigma(r_d) \lesssim 300 t_{i5}$ g cm^{-2}, and the ensemble of observed disk systems yield $1 < \alpha < 1.5$, where $\Sigma \propto r^{-\alpha}$ is the initial surface density distribution in an individual disk. Assuming $\alpha = 1.5$, the surface density in the disks at 1 AU is computed to be $0.7 t_{i5} < \Sigma_0/(1000 \text{ g cm}^{-2}) < 6 t_{i5}$, which is comparable with the minimum solar nebula value of $\Sigma_0 \sim 1000$ g cm^{-2}.

Despite the similarity of these disks with the hypothesized minimum mass solar nebula (Hayashi et al. 1985), it is quite possible that planet formation will be greatly perturbed compared to the current paradigm for planet formation in the solar nebula. Planets can form around low-mass stars in environments like the Orion Nebula only if they accumulate on timescales shorter than the disk destruction timescale. The evaporation process removes disk material beyond $\sim 0.5 r_g$, which is $\sim 1 (M_*/0.2\ M_\odot)$ AU for EUV-dominated evaporation and 10 times this for FUV-dominated evaporation. The accumulation time for massive planets in the outer ($r \gtrsim 5$ AU) solar system is thought to be $\sim 10^7$ yr (Lissauer 1987), longer than the photoevaporation times at these radii for a minimum mass nebula (disk) within 10^{18} cm of stars like θ^1 Ori C. A significant fraction of low-mass stars may have been born in OB associations, probably under conditions similar to what we observe today in Orion. Thus, the outer planets may only form around the fraction of low-mass stars born in more isolated environments. If they do form in the hostile environment of massive stars, they either form from much more massive disks, or they form much more rapidly than current theories predict.

REFERENCES

Bally, J. 1996, Nature, 382, 114

Bally, J., Latter, D., & Devine, D. 1998b, in preparation

Bally, J., Sutherland, R., Johnstone, D., & Devine, D. 1998c, AJ, submitted (Paper I)

Bally, J., Testi, L., & Sargent, A. 1998a, AJ, submitted

Bertoldi, F., & Draine, B. T. 1996, ApJ, 458, 222

Bertoldi, F., & McKee, C. F. 1990, ApJ, 354, 529

Blaauw, A. 1991, in The Physics of Star Formation and Early Stellar Evolution, ed. C. J. Lada & N. D. Kylafis (Dordrecht: Kluwer), 125

Chen, H., Bally, J., O'Dell, C. R., McCaughrean, M. J., Thompson, R. L., Rieke, M., Schnieder, G., & Young, E. T. 1998, ApJ, 492, L173

Churchwell, E., Felli, M., Wood, D. O. S., & Massi, M. 1987, ApJ, 321, 516

Felli, M., Churchwell, E., Wilson, T., & Taylor, G. B. 1993, A&AS, 98, 137

Gagné, M., Caillault, J.-P., Stauffer, J. R., & Linsky, J. L. 1997, ApJ, 478, L87

Garay, G., Moran, J. M., & Reid, M. J. 1987, ApJ, 314, 535

Hartmann, L., Calvet, N., Gullbring, E., & D'Alessio, P. 1998, ApJ, 495, 385

Hayashi, C., Nakazawa, K., & Nakagawa, Y. 1985, in Protostars and Planets II, ed. D. C. Black & M. S. Matthews (Tucson: Univ. of Arizona Press), 100

Henney, W. J., Raga, A. C., Lizano, S., & Curiel, S. 1996, ApJ, 465, 216

Herbig, G. H., & Terndrup, D. M. 1986, ApJ, 307, 609

Hillenbrand, L. 1997, AJ, 113, 1733

Hollenbach, D., Johnstone, D., Lizano, S., & Shu, F. 1994, ApJ, 428, 654

Hollenbach, D., & Störzer, H. 1998, in preparation

Johnstone, D. 1995, Ph.D. thesis, Univ. California, Berkeley
Laques, P., & Vidal, J. L. 1978, A&A, 73, 97
Lissauer, J. J. 1987, Icarus, 69, 249
McCaughrean, M. J., & O'Dell, C. R. 1996, AJ, 111, 1977
McCaughrean, M. J., & Stauffer, J. R. 1994, AJ, 108, 1382
McCullough, P. R., Fugate, R. Q., Chritou, J. C., Ellerbroek, B. L., Higgins, C. H., Spinhirne, J. M., Cleis, R. A., & Moroney, J. F. 1995, ApJ, 438, 394
Mundy, L. G., Looney, L. W., & Lada, E. A. 1995, ApJ, 452, L137
O'Dell, C. R., & Wen, Z. 1994, ApJ, 436, 194
O'Dell, C. R., Wen, Z., & Hu, X. 1993, ApJ, 410, 696
O'Dell, C. R., & Wong, K. 1996, AJ, 111, 846
Parker, E. N. 1963, Interplanetary Dynamical Processes (New York: John Wiley & Sons)

Prosser, C. F., Stauffer, J. R., Hartmann, L., Soderblom, D. R., Jones, B. F., Werner, M. W., & McCaughrean, M. J. 1994, ApJ, 421, 517
Shu, F. H. 1991, Physics of Astrophysics: Gas Dynamics (Mill Valley, CA: Univ. Science Books)
Shu, F. H., Johnstone, D., & Hollenbach, D. 1993, Icarus, 106, 92
Spitzer, L. 1978, Physical Processes in the Interstellar Medium (New York: John Wiley & Sons)
Stauffer, J. R., Prosser, C. F., Hartmann, L., & McCaughrean, M. J. 1994, AJ, 108, 1375
Terebey, S., Chandler, C. J., & André, P. 1993, ApJ, 414, 759
Tielens, A. G. G. M., & Hollenbach, D. 1985, ApJ, 291, 722
Woods, D. T., Klein, R. I., Castor, J. I., McKee, C. F., & Bell, J. B. 1996, ApJ, 461, 767